Title

Spatially-resolved transcriptomics of human dentate gyrus across postnatal lifespan reveals heterogeneity in markers for proliferation, extracellular matrix, and neuroinflammation

Authors

Anthony D. Ramnauth[1,2], Madhavi Tippani[1], Heena R. Divecha[1], Alexis R. Papariello[1], Ryan A. Miller[1], Elizabeth A. Pattie[1], Joel E. Kleinman[1,3], Kristen R. Maynard[1,2,3], Leonardo Collado-Torres[1,4], Thomas M. Hyde[1,3,5], Keri Martinowich[1,2,3,6,+] , Stephanie C. Hicks[4,7,8,9,+], Stephanie C. Page[1,+]

Affiliations

1. Lieber Institute for Brain Development, Johns Hopkins Medical Campus, Baltimore, MD, USA
2. The Solomon H. Snyder Department of Neuroscience, Johns Hopkins School of Medicine, Baltimore, MD, USA
3. Department of Psychiatry and Behavioral Sciences, Johns Hopkins School of Medicine, Baltimore, MD, USA
4. Department of Biostatistics, Johns Hopkins Bloomberg School of Public Health, Baltimore, MD, USA
5. Department of Neurology, Johns Hopkins School of Medicine, Baltimore, MD, USA
6. Johns Hopkins Kavli Neuroscience Discovery Institute, Baltimore, MD, USA
7. Department of Biomedical Engineering, Johns Hopkins School of Medicine, Baltimore, MD, USA
8. Center for Computational Biology, Johns Hopkins University, Baltimore, MD, USA
9. Malone Center for Engineering in Healthcare, Johns Hopkins University, Baltimore, MD, USA

+co-corresponding authors

Correspondence

Keri Martinowich
keri.martinowich@libd.org

Stephanie C. Hicks
shicks19@jhu.edu

Stephanie Cerceo Page
stephanie.page@libd.org

Abstract

The dentate gyrus of the anterior hippocampus is important for many human cognitive functions, including regulation of learning, memory, and mood. However, the postnatal development and aging of the dentate gyrus throughout the human lifespan has yet to be fully characterized in the same molecular and spatial detail as other species. Here, we generated a spatially-resolved molecular atlas of the dentate gyrus in postmortem human tissue using the 10x Genomics Visium platform to retain extranuclear transcripts and identify changes in molecular topography across the postnatal lifespan. We found enriched expression of extracellular matrix markers during infancy and increased expression of GABAergic cell-type markers *GAD1*, *LAMP5,* and *CCK* after infancy. While we identified a conserved gene signature for mouse neuroblasts in the granule cell layer (GCL), many of those genes are not specific to the GCL, and we found no evidence of signatures for other granule cell lineage stages at the GCL post-infancy. We identified a wide-spread hippocampal aging signature and an age-dependent increase in neuroinflammation associated genes. Our findings suggest major changes to the putative neurogenic niche after infancy and identify molecular foci of brain aging in glial and neuropil enriched tissue.

Keywords
hippocampus, neurogenesis, aging, interneurons, extracellular matrix, glia

1 | Introduction

Throughout the lifespan, humans exhibit multiple stages in the development, maturation, and decline of cognitive processes. For example, the capacity to form long term memories does not begin until early childhood [1,2] while cognitive decline begins in late adulthood [3–5] and is accelerated in age-related dementias, such as Alzheimer's Disease (AD) [6,7]. The dentate gyrus (DG) of the hippocampus (HPC) is important for many cognitive functions, including regulation of learning, memory, and mood [8–13]. The development and decline of these critical behavioral functions are tightly linked to anatomical changes in the HPC. The importance of multicellular organization in the HPC is evidenced by the differing patterns of gene expression, morphology, physiology, and connectivity of resident cellular populations [14,15].

The defined circuit structure and canonical cellular composition has rendered the HPC one of the most highly studied brain regions in both humans and model organisms. While functional and anatomical differences between species exist [16], the extent of these differences remains unclear, as illustrated by the ongoing controversy surrounding the existence, abundance, and function of postnatal hippocampal neurogenesis in the human brain [17]. Postnatal neurogenesis and the various cell types that are characteristic of the developmental trajectory from radial glial-like cells to immature granule cells (imGCs) have been well described in the mouse using single-cell RNA sequencing (scRNA-seq) [18]. Additionally, single nucleus RNA sequencing (snRNA-seq) experiments in macaque tissue identified neural precursors and characterized gene markers that are conserved and unique to these non-human primates when compared with mice [19]. The majority of evidence supporting the existence of adult neurogenesis in the human HPC comes from immunohistochemical or other antibody-based assays [20–28]. Studies using snRNA-seq in the human HPC suggest a paucity or absence of granule cell neurogenesis in the adult, but they do however support the possibility of GABAergic adult neurogenesis [29,30]. Limits to interpretation in these snRNA-seq studies stems from the fact that the generated molecular profiles fail to capture extranuclear transcripts, which are important for physiological processes relevant to neural differentiation and maturation, including local translation at synaptic terminals [31–33]. This is particularly important since the molecular layer (ML) contains many neurites from the granular cell layer (GCL). Laser-capture microdissection (LCM) retains some spatial specificity and can capture extranuclear transcripts, but it hinders ability to examine spatial relationships within intact tissue [34]. Interestingly, transcriptional profiles obtained with LCM across the human lifespan in the GCL identified GCL-specific gene expression associated with aging that was not detected in RNA-seq data from the whole HPC [35,36]. These discrepancies highlight the importance of retaining anatomical topography while capturing cytoplasmic transcripts to understand human-specific aspects of neurodevelopment and age-related disorders in the HPC.

Compared to other brain regions, the HPC is particularly sensitive to the effects of development and aging. Humans exhibit infantile amnesia in the early stages of life, which is hypothesized to correlate with prolonged postnatal neurogenesis in the DG [37–41]. Conversely, in the latter part of life, the HPC is vulnerable to neurotoxic effects of "inflammaging" - an age-related increase in the levels of pro-inflammatory markers. Human functional magnetic resonance imaging (fMRI) studies suggest that blood-brain barrier (BBB) permeability increases with age in the HPC and is more pronounced in the DG [42]. Aged rodent neuroblasts display a senescence-associated secretory phenotype that induces an auto-inflammatory response [43], and glial cells, including microglia and astrocytes, undergo senescence or age-dependent dysregulation in the DG, resulting in decreased neurogenesis and exacerbation of neurodegeneration [44–53]. In fact, activated microglia can induce reactive astrocytes [47], which may further inflammation and neurodegeneration. Importantly, gene expression changes found in aged mice do not fully recapitulate the expression phenotype of aged human microglia [54], which makes human post-mortem studies extremely valuable. Additionally, mature oligodendrocytes also show shifts in gene expression correlated to aging in the white matter (WM) of rodents [55]. These findings highlight the importance of analyzing both neuronal and non-neuronal cellular populations across species in aging.

In this study, we generated molecular profiles for spatial domains of the human DG, and analyzed gene expression patterns in these domains across the postnatal lifespan. Specifically, we used spatially-resolved transcriptomics (SRT) to generate an atlas of spatial gene expression in the human DG at four stages across the lifespan from infancy to the elderly. This experimental design facilitated the retention of cytoplasmic transcripts while preserving the spatial topography of the DG. We performed differential expression analyses across age groups at the level of (i) whole DG and (ii) individual DG sub-domains. We also provide an interactive web application of this data (https://libd.shinyapps.io/Lifespan_DG/) to enable further exploration of molecular heterogeneity in the DG across the postnatal lifespan.

2 | Results

2.1 | Experimental design and overview of spatially-resolved molecular profiling within the dentate gyrus across the postnatal lifespan

We collected tissue blocks from 17 neurotypical donors spanning ages 0.18 years to 76.7 years (**Table S1**) to characterize spatial gene expression within the DG using the 10x Genomics Visium Spatial Gene Expression platform (**Figure 1a**). To increase the ability to detect distinct molecular signatures across the lifespan we focused on distinct age brackets, rather than age as a continuum, and thus binned donors into four groups: infant (0-2 years), teen (13-18 years), adult (30-50 years), and elderly (70+ years). Tissue blocks were dissected from coronal slabs of fresh-frozen postmortem human brains at the level of the anterior hippocampus. Each block was scored to isolate the DG, and cryosections were mounted on Visium slides (total of *N*=17 capture areas), with each capture area containing a unique donor from a specific age group. Following image acquisition and sequencing, we performed quality control (QC) (Methods 4.2, 4.6, **Figures S1-S2**) to assess the quality of the generated libraries and qualitatively confirm DG inclusion on each capture area from each donor. We removed donor Br3874 because it did not contain GCL (**Figures S2-S3**), and hence, we retained a total of *N*=16 capture areas with a total of 68,685 spots for downstream analysis. Finally, we preprocessed the Visium data to perform normalization, feature selection, and data integration using *Harmony* [56] to correct for batch effects (**Figure S4**).

To take advantage of the high-dimensional nature of the data, we performed data-driven unsupervised clustering. Using *BayesSpace* [57], *k*=10 predicted spatial domains (**Figure 1b**) that expressed canonical spatial domain-specific and neuropil-enriched gene markers (**Figure 1c**). These 10 spatial domains qualitatively overlap with canonical HPC regions as demarcated by H&E staining as well as histologically- and marker gene-guided manual annotations (**Figures S5-S8**). Domain 7 is enriched for canonical GCL markers *PROX1* and *CALB1* , domain 6 is enriched for interneuron markers characteristic of the subgranular zone (SGZ) including *GAD1*, *GAD2*, and *SST*, domain 2 is enriched for synaptic markers such as *CAMK2A* and mitochondrial gene *MT-ND6* characteristic of the ML, and domain 4 is enriched for regional markers of cornu ammonis 3 (CA3) and CA4 including *KIT* and *TRHDE* (**Figures 1c, S8**). Spatial domains from other HPC regions besides the DG and SLM (cluster 1), were not well-centered on each capture area, and thus these domains were not equally represented in all donors (**Figure S6**). From visual comparison with H&E staining and manual annotations, *BayesSpace* did not resolve CA3 from CA4 at *k*=10, so domain 4 was classified as 'CA3&4' (**Figures S5-S6**). Comparison of these predicted domains to manual annotations of Visium spots (**Figure S9a, Table S2**) reveals less intermingling of spot labels in expression space as visualized using principal components (PC) and Uniform Manifold Approximation and Projection (UMAP) (**Figures S9b-S9c**). We also calculated the proportion of spot cluster label intermingling by computing the cluster neighborhood purity [58] and found higher purity in the predicted domains than in manual annotations (**Figure S9d**). Therefore, we proceeded using the predicted spatial domains as defined by *BayesSpace* for downstream analysis.

To reduce the sparsity of UMI gene counts within predicted spatial domains, we followed a previously published workflow for pseudo-bulking Visium spots [34] by summing the UMI counts of each gene for each capture area across spots within a spatial domain (**Figure 1d**). This improves the ability to estimate log fold changes when comparing spatial domains or comparing age groups within a given spatial domain. Using the 160 pseudo-bulked samples (16 capture areas x 10 spatial domains), we perform principal components analysis (PCA) and found that the choroid plexus (CP) domain (cluster 3, **Figure 1c**), a secretory tissue that produces cerebrospinal fluid, compared to non-CP domains explained the largest fraction of variation in several principal components (**Figure S10a**). Based on this data, we removed that pseudo-bulked spatial domain from our downstream analysis and repeated PCA. As a result, PC1 was associated with spatial domains while PC2 was associated with age, specifically infant versus non-infant samples (**Figures 1e, S10b**), highlighting a distinction in expression space between infants and the other age groups.

2.2 | Differential expression analysis identifies age-associated genes in the dentate gyrus

Using the pseudo-bulked data, we combined the predicted ML, CA3&4, SGZ, and GCL spatial domains to generate a composite DG (**Figure 2a)**. We next performed differential expression (DE) analysis across the four age bins to identify age-associated genes in the DG (**Table S3**). The largest number of differentially expressed genes (DEGs) was identified when comparing the infant (or elderly) age groups to all others, while fewer DEGs and smaller fold changes were found when comparing the teenage and adult age groups (**Figures 2b-e**). Interestingly, we note a reversal of significant fold changes starting in the adult group with respect to proliferative genes and immune-related genes. Specifically, some genes associated with neurogenesis were only significantly upregulated in infant groups, while activated microglia and reactive astrocytes were downregulated in the infant and teen groups (**Figures 2b-c**) but upregulated in the adult and elderly groups (**Figures 2d-e**). This pattern suggests an inverse relationship between proliferative potential and glial inflammatory activity. We also noted depletion of some GABAergic marker genes in the infant versus others group, which were significantly enriched in the adult group; specifically *LAMP5* and *CCK* (**Figures 2b, 2d**). Gene ontology (GO) analysis suggested increased proliferation in the infant group compared to all the other age groups and enhanced immune-related activity in adulthood continuing into old age (**Figure 2f, Table S4**). We observed a repeated upregulation in the infant and elderly group for only one GO term associated with proliferation: gliogenesis. GO terms for respiration-related processes are increased in the adult group, suggesting increased oxidative stress, which could drive senescence and inflammation while inhibiting proliferation [50,59–61]. However, those GO terms do not remain elevated in the elderly group. Another potential driver of inflammation is BBB disruption [50,62,63]. The GO term for BBB maintenance is increased in infancy, while the GO term for response to ischemia is decreased in infants and increased in elderly groups, suggesting deterioration of the vasculature with age. There are also a set of reversals in GO terms from infancy to old age related to development of synapses and dendrites, lysosomal membrane, synapse pruning, and the major histocompatibility class II (MHC-II) immune response; the latter three suggesting increased microglial activity (**Figure 2f**).

2.3 | Selective proliferation and extracellular matrix organization in infancy with continued neuroblast signature into old age

We next investigated differential expression across the lifespan in sub-domains of the DG. Specifically, we conducted pseudobulked DE analysis within each predicted spatial domain across the 4 lifespan stages.

Although many of the same genes are significantly enriched or depleted as in the entire DG, there are important regional differences that map to specific sub-domains of the DG. Interestingly, several genes associated with interneuron subtypes or interneuron function are depleted in the infant group: *GAD1* in ML and GCL, *LAMP5* in ML, GCL, and SGZ, and *CCK* in all DG spatial domains (**Figures 3a-d, Table S5**). Surprisingly, spatial visualization for *LAMP5* shows prevalent expression in the GCL, which is primarily composed of excitatory neurons, after infancy (**Figure S12a**). We qualitatively validated these changes at the GCL in *GAD1* and *LAMP5* using RNAscope in infant and adult donors (**Figure 3e**). Supporting this finding, we queried a bulk RNA-seq dataset, which contained HPC from infant to elderly samples [35], and observed increased *LAMP5* expression with aging (**Figure S12b**). We also compared this bulk HPC RNA-seq dataset with a LCM RNA-seq dataset of the GCL, which used a partially overlapping set of donors and spanned the teens to elderly age group [35,36] and found enrichment of *LAMP5* in the GCL relative to bulk HPC (**Figure S12c**). *CCK* expression shows a similar increase after infancy in both this dataset (**Figure S13a**) and in the bulk HPC RNA-seq dataset (**Figure S13b**), but, unlike *LAMP5,* is enriched in the SGZ and CA3&4. We also observed significant depletion of pan-glial gene expression in infancy, including genes typically expressed in oligodendrocytes and astrocytes such as *GFAP* in ML, GCL, and CA3&4; *TMEM176* in ML, SGZ, and GCL; *S100A1, S100A13,* and *PTGDS* in all DG spatial domains; and *HHATL* in ML, GCL, and CA3&4 (**Figures 3a-d, Table S5**).

DE comparison of infant versus non-infant yielded the most DEGs for all the spatial domains (**Figure 3f, Figure S11, Table S5**). We ruled out that this finding is a function of sampling more spots, UMIs, or detected number of genes (**Figure S14**). However, we do note a decreasing trend in nuclei density per Visium spot in the GCL (**Figure S15**). This could not be incorporated in our modeling as nuclei segmentation data was only available from two Visium slides. We also investigated DEGs for the teen (**Figure 3f, Table S5**), adult (**Figures 3f, S16a-d, Table S5**), and elderly groups (**Figures 3f, S16e, Table S5**). Interestingly, we found no significant DEGs for teen compared to non-teen, but we do however note that this DE analysis may be underpowered to detect differences. Combining the top DEGs from the infant compared to non-infant DEGs for all four spatial domains in the DG, we visualized gene expression gradients across age for each DG spatial domain (**Figure 3g**). This visualization illustrates rapid changes in expression after infancy of this subset of genes, which includes many canonical neurodevelopmental markers including *SOX4*, *SOX11*, *WNT5A*, *IGFBP2*, and *DPYSL5,* whose expression declines with age. In agreement with findings from snRNA-seq in human HPC [29], we found that *METTL7B,* was one of the top significantly depleted genes in infancy. *METTL7B* expression was depleted in the infant ML and SGZ, but then increased with age (**Figure 3g, S17**). Expression of *DCX*, a widely used marker of adult neurogenesis in the GCL, rapidly decreased beyond infancy. In fact, spatial visualization of *DCX* expression illustrates low expression levels in the GCL that rapidly decrease with age (**Figure S18a**). Querying the previous bulk HPC RNA-seq dataset [35] supported the rapid decrease of *DCX* expression over age (**Figure S18b**).

In addition to identifying DE genes, we investigated changes in estimated cell proportions for *LAMP5* interneurons, oligodendrocytes, and astrocytes using one of the largest publicly-available human HPC snRNA-seq reference datasets [29] (**Figure S19**) and *cell2location* [64], a method for cell type deconvolution [65] (**Figures S20-S21**). *Cell2location* estimated an increase in proportion of *LAMP5* interneurons after infancy, particularly in SGZ and CA3&4 (**Figure S22a**), oligodendrocytes in ML, SGZ, and CA&4 (**Figure S22b**), and for both subtypes of astrocytes (Astro_1, *GFAP*$^{+}$ and Astro_2,*GFAP*$^{-}$) in the ML and SGZ (**Figures S22c-d**). The data suggest that although infancy is generally a period of increased proliferation, proliferation of some cell types occurs after infancy.

In agreement with upregulation of the GO term for ECM organization in the infant group (**Figure 2f**), we found significant enrichment of many ECM-related genes in infant ML, SGZ and GCL, including *POSTN*, *PTN*, *WIF1*, *COL1A2*, *BCAN*, *COL6A1*, *HAPLN1*, *SERPINH1*, and *NPNT* (**Figures 3a-d, Table S5**). *POSTN,* which

encodes a cell adhesion molecule (periostin) that is implicated in hippocampal neurogenesis in rodents [66], is spatially enriched in the infant GCL, and declines across aging (**Figures 3b, 3d, S23**).

Since many proliferative markers are enriched in the infant group but decrease with age, we queried previously collated gene sets representing discrete stages of neurogenesis from animal and human scRNA-seq and snRNA-seq studies. Specifically, we examined gene sets identified from three different studies: three gene sets from a scRNA-seq study of mouse DG spanning postnatal day 12 to day 35 for neuronal intermediate progenitors (nIPC), neuroblast type 1 (NB1), and NB2, a gene set of shared markers with the above mentioned mouse study and a scRNA-seq study of adult macaques for neuronal progenitor cells (NPC), and two gene sets [one shared with mouse and one unique to human] from a snRNA-seq study of human immature granular cells (imGC) from prenatal to 92 years old [terminology adopted from each publication] [18,19,67]. One gene set consistently showed significant enrichment in the GCL for all age groups: mouse late-stage neuroblasts (NB2) (**Figure 4a**). In the developmental trajectory of hippocampal neurogenesis and differentiation from rodent models, the NB2 stage is characterized by the cessation of proliferation and the initiation of differentiation into neurons [18]. When we examine genes in the N2B gene set, we find that many of these genes are widely expressed throughout the DG, as opposed to restricted to the GCL/SGZ (**Figure 4b, S24**). These results suggest that the majority of these mouse-derived markers may be non-specific for canonical adult neurogenesis of human granule cells. However, some genes are preferentially enriched in the GCL, including *BHLHE22*, *PPFIA2*, *SEMA5A*, *RASL10A*, and *SEMA3C* (**Figure 4b, S24**). Visualization of spatial gene expression within the HPC for two canonical neuroblast markers from the NB2 gene set - *BHLHE22* and *NEUROD2* - shows expression in the GCL as well as other neuron-rich spatial domains across all four ages groups (**Figures 4c-d**). Interestingly, the gene sets for immature granular cells (imGCs) (both shared with mice and those exclusive to humans), derived from a machine learning-based analytical approach trained on snRNA-seq data, showed more enrichment in the CA3&4 spatial domain compared to any other domain, and enrichment decreased to non-significance in the elderly group (**Figure 4a**). This data suggests that genes that were identified as markers for neural differentiation in mouse studies are expressed in the human HPC throughout the lifespan, but do not appear to be specific markers of imGC proliferation within the GCL. This data also highlights the limitations of training machine learning algorithms only on snRNA-seq data.

2.4 | A minimal gene set tracks wide-spread hippocampal tissue changes with aging

Given the strong age-associations from many gene markers of, for example proliferation and inflammation (**Figure 2**), we then asked if a minimal set of these genes can be used to assay which spatial domains change the most with age. To this end, we adapted a previously published, data-driven workflow [55] that used a set of DEGs produced by comparing older age groups to the youngest group (in our case, infant) in order to compute a common aging score (CAS) for bulk RNA-seq, scRNA-seq and Visium in the mouse brain throughout postnatal life. Each CAS is a single-valued summary of the contrast between transcriptional programs that represent biological conditions: in our case younger versus older age conditions. To control for possible differences in cell types across spatial domains, we performed differential expression within each pseudo-bulked spatial domain (excluding CP) for each non-infant age group compared to the infant group. Genes were selected based on thresholds of adjusted *p*-values smaller than 0.05 and a $\log_2$ fold change of at least 1.5 in at least two of the differential expression tests and were shared with at least 3 spatial domains. This resulted in a minimal, signed (+/-), gene set of 46 positively and 13 negatively associated genes to aging relative to the infant group (**Table S6**). Some of the wide-spread aging DEGs show decreasing expression of proliferative markers such as *DCX*, *SOX11*, and *SOX4*, with an increased expression of genes for oligodendrogenesis such as *MAL* and *OPALIN*, or MHC class II associated inflammatory signaling genes, such as many *HLA* genes (**Figure 5a, S25**). GO analysis suggested downregulation of neural proliferation,

upregulation of inflammatory activity and myelination, and both upregulation and downregulation of subsets of genes associated with gliogenesis and oligodendrogenesis (**Figure 5b**) similar to previous comparisons within the DG across all age groups (**Figure 2**).

Using this wide-spread aging gene set as input, we employed the *Vision* package [68] to compute the CAS per Visium spot for all of our Visium capture areas (**Figure S26**). First, we investigated the relationship between CAS scores and the predicted proportion of cell types at each spot to assess if changes in cell type proportions were associated with changes in CAS scores. Using the predicted *cell2location* mean abundance estimates, we applied PCA to extract top PCs that explained the most variation per spot, following a similar workflow [69]. While we found a relationship between the spot-level CAS scores and spot-level predicted cell type proportions (PCs 1-4 explained 38% of the variation), particularly for oligodendrocytes, differences in the predicted cell type proportions were not sufficient to explain the majority of the variation in CAS scores (**Figure S27**). We note that the identified relationship for oligodendrocytes is not due to differences in the proportion of collected WM spots in infants (**Figure S7**), but rather may be driven by increases in oligodendrogenesis, which are documented as increasing in animal models following infancy [70]. When CAS values for individual Visium spots are organized by age and spatial domain we found that the trajectory rapidly increased from infancy to the teenage years for all HPC spatial domains, but the increases in scores and variability of scores were larger in glial- and neuropil-enriched Visium spots relative to neuron-enriched spots (**Figure 5c**), accurately summarizing the changes in expression for genes from the aging gene signature (**Figure 5a**). Spatially, spots within WM have the largest CAS value changes relative to other Visium spots, but show heterogeneity in scores even within WM regions (**Figures 5c-5d, S28**). Comparing our CAS values to values derived from the whole-brain aging gene set in the original mouse study [55] highlights the importance of having an infant group. In the mouse whole-brain study, the youngest age group was 3 month old mice, which correlates approximately to humans in their mid-twenties [71,72]. As a result, although we do see a similarity in spatial assignment of CAS values (**Figure S28a**), our values were more sensitive to Visium spots rich in oligodendrocytes (**Figure S26-S27, S28b**). It is important to note that our DEGs and CAS results could not take into account cell density changes per Visium spot with age (**Figure S15**), which have decreasing trends for the GCL and increasing trends for WM.

As previously demonstrated [55], approximating the CAS trajectories with linear modeling (**Figure 5e**) allowed us to use the slope to infer a “CAS velocity” for each spatial domain. With these slopes we approximated which HPC spatial domains exhibit a higher rate of aging-associated changes (captured by our gene set) compared to other spatial domains. Similar to Visium data from mice, even though the DEGs are relative to infancy in our case, the CAS baseline (i.e. CAS assigned to the infant Visium spots) did not strongly predict a spatial domain’s CAS velocity across age (**Figure 5f**). Comparing the CAS velocities for each HPC spatial domain suggests that glial enriched spatial domains have the largest CAS velocities, followed by neuropil enriched spatial domains (**Figure 5g**). This is in agreement with previously mentioned work showing that more age-associated changes were observed in glial-rich regions, including WM. Of note, the most neuropil-enriched spatial domain of the DG, the ML, had a significantly larger CAS velocity than any of other DG sub-domains.

2.5 | Neuroinflammatory activity is a robust signature of aging in many regions of the hippocampus

We identified antigen processing and presentation of peptide or polysaccharide antigen via MHC class II as a GO term that was inversely expressed between the infant and adult group in the DG, with persistent upregulation in the elderly group (**Figure 2f**). We also observed many genes associated with MHC class II inflammatory signaling in our wide-spread aging gene set (**Figure 5b, Table S6**). Since MHC-II peptides are highly expressed by late-stage activated microglia [49], we investigated the spatial heterogeneity of markers for activated microglia in the DG throughout the lifespan by performing spatial gene set enrichment analysis on

gene sets derived from activated microglia [49,73] across the spatial domains from all samples. Genes associated with late-stage activated microglia were enriched in neuropil- and WM-rich spatial domains outside of the DG, especially the SLM (**Figure 6a**). The SLM is well-represented in nearly all Visium capture areas and thus can be included in our differential expression tests (**Figures S6-S7**). Many genes that comprise the MHC-II immune response show an age-dependent increase in expression in DG and SLM spatial domains (**Figure 6b**). Although *CD74* is not significantly enriched in the individual spatial domains, it is enriched in the composite DG of the elderly group (**Figure 2d),** and its expression increases with age (**Figure S29a**). We also find an increase in its expression in the previous bulk HPC lifespan data (**Figure S29b**). Importantly, we observe upregulation of genes such as *C1QB* and *IL4R* that are included in core signatures of microglial markers derived from human snRNA-seq studies [54] when comparing elderly versus non-elderly ML and CA3&4 (**Figures 6d, f**). We also note that, although not significantly enriched in any specific DG spatial domain, the canonical microglial marker *TREM2* is enriched in the composite DG of the adult and elderly groups (**Figures 2d-e**). Activated microglia can induce reactive astrocytes [47] and we detect enrichment of genes markers for reactive astrocytes such as *CD14* in ML, SGZ, CA4&3, and SLM, and *S100A10* in the ML (**Figures 6c, 6f**). In the composite elderly DG, we also detect enrichment of other reactive astrocyte markers such as *GFAP*, *C3*, *SERPINA3*, *EMP1*, *CD109*, *CD44*, *SERPING1*, and *FKBP5* (**Figure 2e, Table S3**).

One of the most enriched transcripts in the elderly SLM is *HAMP* (**Figure 6c**), which encodes hepcidin and is important for iron storage in microglia, astrocytes, and neurons. While it is not significantly enriched in any individual spatial domain comprising the DG, it is enriched in the composite DG in the elderly group (**Table S3**). Inflammatory stimuli can induce iron accumulation in microglia and neurons *in vitro* via hepcidin and related molecules [74], which is important because iron overloading is consistently observed in aging microglia that express a senescent or dystrophic phenotype [51,52].

Interestingly, we observe a variety of immune-related gene expression. Some of the observed genes are expressed in activated human microglia, while others are also found in immune-related cell types (*FCGR1A-3A*). For example, *FCGR3A*, which shows enrichment in ML, SGZ, CA3&4, and SLM (**Figures 6c, 6f**), is important for survival and proliferation of natural killer (NK) cells[75,76], which are recruited by aged neuroblasts in the rodent HPC, and contribute to impaired adult neurogenesis [43]. *cell2location* cell type deconvolution estimated an increasing proportion of microglia in the SGZ with age (**Figure S30a**), followed by a similar pattern for T-cells (**Figure S30c**). While NK cells, T-cells and microglia share some overlapping transcriptional signatures, the extent of overlap, particularly in humans, is unclear. *FCER1G*, a gene enriched in the elderly SLM and CA3&4, is a part of the MHC II immune response and has previously been detected in both microglia and NK cells [77–80]. There is conflicting evidence regarding the presence of invasive immune cells in the HPC as the result of BBB disruption or local proliferation [43,81–83]. It is important to note that, in our data, *SERPINA3*, a reactive astrocyte marker upregulated in the elderly DG (**Figure 2d**), is involved in BBB disruption through astrocytic activity [84]. Additionally, we observed that the response to ischemia GO term was downregulated in the infant groups and upregulated in the elderly group (**Figure 2e**), supporting the notion of BBB disruption with aging.

3 | Discussion

In summary, we identified several changes to the molecular topography of the human DG that are unique to specific life stages by assaying spatial gene expression across the postnatal lifespan. In infancy, we observed selective increases in proliferative markers and enrichment of ECM-related genes. To determine which spatial domains of the HPC were most susceptible to age-related changes, we calculated DEGs across age-groups relative to infancy, and found that these genes correspond to glial- and neuropil-rich domains. Over the lifespan, these regions were also enriched for expression of genes associated with inflammatory signaling in

glial populations. Our data also suggest that other populations of immune cells, such as NKs, may be involved in “inflammaging”. Although we detected a molecular signature of neuroblasts that were localized to the GCL and throughout the lifespan, many of the genes comprising this neuroblast signature were not exclusive to the GCL, and we did not observe other published neurogenesis-related gene sets at the GCL beyond infancy. Depletion of inhibitory markers in the infant group suggests delayed development or migration of *GAD1*$^{+}$, *LAMP5*$^{+}$, and *CCK*$^{+}$ neurons in the human HPC. Finally, our data is made fully available as a neuro-resource for further exploration and investigation.

To date, most high-throughput transcriptomics of the human HPC across development and aging have been limited to bulk RNA-seq, laser-capture, or snRNA-seq studies [29,30,35,36,67,73]. For bulk or laser-captured tissue, studies become constrained by experimental microdissections, which for some small regions can be difficult to isolate or sparse in transcripts. Due to the large size and relative fragility of human neurons, and because most available postmortem human tissue is frozen, whole cell preparations for single cell applications are difficult or infeasible. Hence, most studies have been conducted with snRNA-seq [34], which unfortunately lacks spatial information, and does not contain transcriptomic information from cytosolic compartments, such as neuronal processes. In addition, variations in sample preparation workflows can bias against preservation of some cell types or can affect expression profiles [85–88]. Some SRT technologies are based on variations of single-molecule fluorescent *in situ* hybridization (smFISH), which is considered the gold standard for validating the spatial localization of transcripts [89]. However, although technologies to label hundreds to thousands of transcripts have recently been developed, limitations to these strategies include intracellular molecular crowding, limited number of fluorescent markers, and the time- and labor- intensive nature of these strategies [90,91]. In the human hippocampus, accuracy of nuclear and transcript segmentation is critical given the density of neurons, and controlling for the effects of confounding lipofuscin auto-fluorescence, particularly over aging, is challenging. To obtain transcriptome-wide resolution, while retaining cytosolic transcripts and spatial accuracy, we used the 10x Genomics Visium Spatial Gene Expression platform. This allowed us to leverage deep sequencing and imaging-based spatial coordinates for the DG beyond the nucleus. As an example, previous snRNA-seq studies were unable to detect age-related changes to *GFAP*+ astrocytes in the ML [73], whereas here, we resolve an age-dependent increase for some astrocyte markers in the ML. We used cell type deconvolution to infer a possible age-dependent increase in cell abundance for *GFAP*+ astrocytes within the ML. Additionally, we were able to show an enrichment of age-related changes in the ML compared to other spatial domains of the DG.

While the Visium platform allowed us to capture non-nuclear transcripts within the intact tissue architecture to fill epistemic gaps in our understanding of differential age-related changes in the HPC, there are important limitations to our experimental design. The biggest limitation is sample size, as evidenced by fewer DEGs resulting from age comparisons with teen and adult age groups. More technical caveats include the comparatively large size of Visium spots (55 µm diameter), being limited to H&E staining to define histology as opposed to alternative staining methods that could provide orthogonal measures of cellular structure, absence of nuclei segmentation for some samples, and being limited to transcriptomic information as opposed to proteomic information. Given the relatively large spot diameter, Visium spots can contain multiple cell types and a heterogeneity of cell density. Thus, age-related statistics, such as the CAS values, are subject to cell compositional and abundance changes and do not represent a truly cell-independent signature of aging. Future experiments using *in situ* hybridization and immunofluorescence methods can be designed to further investigate the age-related changes we detected at cellular resolution.

Cellular-resolution transcriptomic technologies will be useful to validate and further characterize the development of certain cellular populations, including *GAD1*$^{+}$, *LAMP5*$^{+}$, and *CCK*$^{+}$ cells during infancy and post infancy. This is especially important since our data suggests that some GABAergic markers, such as *GAD1*, are enriched at the GCL, a layer primarily composed of excitatory neurons, along with late-stage neuroblast

markers into old age. This trend is not detected for the other cell types that make up the developmental trajectory of granule cell neurogenesis, and supports previous findings from other studies. For example, overlap of DCX with GAD1 was reported using immunohistochemical techniques in the adult GCL [29], suggesting the possibility of prolonged interneuron development rather than the presence of imGCs in human GCL. In the case of LAMP5, since LAMP5 protein is localized to GABAergic axon terminals, mRNA may be trafficked and locally translated at GCL synapses as opposed to cell bodies of *LAMP5*$^{+}$ interneurons being located at the GCL [92]. However, these data do not rule out the possibility of increased *LAMP5*$^{+}$ interneuron proliferation in the GCL or SGZ. Since *LAMP5*$^{+}$ interneurons tend to have smaller neuronal arbors than other interneurons [93] the presence of their transcripts suggests spatial proximity of their nuclei. Another possibility is that expression of *LAMP5* in human GCs may increase with age. Interestingly, *LAMP5*$^{+}$ excitatory neurons are found in layer 2/3 of the human cortex and in the basolateral amygdala, with both inhibitory and excitatory subtypes having higher abundance in humans as compared to mice [94,95]. Therefore, it is important to further investigate *LAMP5* expression quantitatively in the DG to determine whether our results arise from increased *LAMP5* expression within already expressing cells, expansion of the *LAMP5* expression in previously non-expressing cells, or proliferation of a specific cell type with age. This has implications for functional studies since reducing expression of LAMP5 in mice reduces odor discrimination [92], while LAMP5 reduction in AD mice models show increased hyperexcitability in HPC and further impairs spatial learning and memory formation [96].

The increased abundance of markers for ECM molecules that we observe in the infant DG suggests that they may play a role in supporting the neurogenic niche. Many of these genes are associated with brain development, but remain understudied. For example, *WIF1* is important for rodent brain development [97,98], and *PTN* is upregulated in tandem with increases in adult neurogenesis following exposure to environmental enrichment in a mouse model of senescence [99]. *PTN* overexpression, or pharmacological activation of AKT signaling downstream of the PTN receptor, PTPRZ1 (note that *PTPRZ1* expression in the DG decreases with age in our data (**Table S3**)), ameliorates aging-related neurogenesis declines in this same model of senescence [100]. *HALPN1,* which encodes hyaluronan and proteoglycan link protein 1, is important for the maturation of perineuronal nets surrounding PV+ interneurons in the mouse dorsal CA1, which affects neuronal allocation and memory precision [101]. In the context of HPC neurogenesis, neural stem cell proliferation and differentiation into neurons and astrocytes increases *in vitro* after adenovirus transduction with *POSTN*, while transduction of *POSTN* into the lateral ventricles of neonatal rat brains stimulated proliferation and differentiation in the SGZ, but only after hypoxic-ischemic brain injury [66]. Given its importance in rodent HPC development and its enrichment in human infant HPC, assaying changes to the ECM's composition, density, and localization with age in a spatial domain-specific manner can provide insight into strategies to manipulate cellular proliferation in humans.

We also note that inflammatory signaling increases with age in our data. Genes associated with neuroinflammation constituted a large portion of our CAS, and were enriched when comparing the elderly group to all other age groups. However, it is important to identify inflammatory markers with little to no overlap in microglia and other immune cells, such as NK cells. Our data is also inconclusive as to whether invasive immune cells are present as a result of BBB disruption. Since locally proliferating NK cells affect adult neurogenesis in mice [43], it would be interesting to examine if this phenomenon is limited to NK cells. *CD74* is expressed by microglia, but CD74 protein is also detected in Aβ plaques and neurofibrillary tangles in the HPC of brain donors diagnosed with Alzheimer's (AD), suggesting neuronal expression of *CD74* [102]. In fact, overexpressing *CD74* decreases Aβ production in CA1-3 pyramidal neurons in an AD mouse model, and in *in vitro* fetal human neurons [103]. We detected a small, but significant, depletion of *APP* in infant DG, and enrichment in elderly DG (**Table S3**). Although CD74 expression has been observed in pyramidal neurons in the HPC, this evidence is limited to immunohistochemical labeling [102–104], and has not been reported in the human DG. Since *CD74* is involved in neuroinflammation and proteinopathies, identifying the cellular origin of increased *CD74* expression across aging is important.

A major limitation to studies with human brain tissue is an inability to investigate causality. However, several findings from this study can be directly tested in rodent models. For example, investigating the physiology of orthogonal *GAD1*$^{+}$, *LAMP5*$^{+}$, and *CCK*$^{+}$ interneuron subtypes in mice can elucidate the timing and functional changes of critical periods in the early development of the HPC due to changes in circuit physiology. Given mouse studies that reveal LAMP5's importance for HPC excitability, as well as spatial memory and learning, manipulating *LAMP5*$^{+}$ interneurons at the GCL/SGZ may elucidate how processes important for learning and memory, such as pattern separation by inhibitory gating or filtering, changes with age. Modulating the expression of genes such as *POSTN* in perinatal and adult mice could elucidate the role of the ECM in the DG neurogenic niche by revealing how the milieu of ECM and neurogenic signaling evolves with time. CD74 expression could also be manipulated in a spatial domain-specific and age-specific manner to dissect its role in neuroinflammatory signaling and Aβ load in the DG. Microglia show a robust cellular signature of aging in the DG, and thus may represent a promising target for future manipulation studies. Our data contributes to existing evidence that aged/senescent/dystrophic microglia accumulate throughout the DG and SLM across aging. Using alternative methods such as iron staining can help confirm that these are indeed aged/senescent/dystrophic microglia, and future strategies to perturb this accumulation can ascertain their potential relationship with reactive astrocytes in the human brain. Aged microglia may be a promising target for future therapies in age-associated neurodegeneration and cognitive decline.

4 | Methods

4.1 | Tissue samples

Postmortem human brain tissue from male and female neurotypical donors of European and/or African ancestry spanning ages 0.18 years to 76.7 years were obtained by brain donations (*N*=17) collected through the following locations and protocols at the time of autopsy: the Office of the Chief Medical Examiner of the State of Maryland, under the Maryland Department of Health's IRB protocol #12–24, the Departments of Pathology at Western Michigan University Homer Stryker MD School of Medicine, the University of North Dakota School of Medicine and Health Sciences, and the County of Santa Clara Medical Examiner-Coroner Office, all under WCG IRB protocol #20111080. One additional sample was consented through the National Institute of Mental Health Intramural Research Program (NIH protocol #90-M-0142), and was acquired by LIBD via material transfer agreement, all with informed consent from the legal next of kin. All donors here were negative for illicit drugs of abuse. Demographics for the 17 donors are listed in **Supplementary Table S1**. Clinical characterization, diagnoses, macro- and microscopic neuropathological examinations, were performed on all samples using a standardized paradigm; and then subjects with evidence of macro- or microscopic neuropathology were excluded. Details of tissue acquisition, handling, processing, dissection, clinical characterizations, diagnoses, neuropathological examinations, RNA extraction and quality control (QC) measures have been described previously [105]. Briefly, the anterior half of the HPC containing dentate gyrus was microdissected using a hand-held dental drill as previously described [35], staying within the anterior half of the HPC as guided by visual inspection of the HPC itself and up to visual presence of the lateral geniculate nucleus and shrinkage of the putamen. Tissue blocks were then stored at -80°C.

4.2 | Tissue processing and quality control

Frozen brain blocks were embedded on the posterior end in OCT (TissueTek Sakura) and cryosectioned at −10°C (Thermo Cryostar). Brain blocks were cryosectioned and stained with hematoxylin and eosin (H&E) to verify the presence of anatomical landmarks of the dentate gyrus such as the GCL. Sections were placed on

chilled Visium Tissue Optimization Slides (catalog no. 3000394, 10x Genomics) and Visium Spatial Gene Expression Slides (catalog no. 2000233, 10x Genomics), and adhesion of tissue to slide was facilitated by warming the back of the slide. Tissue sections were then fixed in chilled methanol, and stained according to the Methanol Fixation, H&E Staining & Imaging for Visium Spatial Protocol (catalog no. CG000160 Rev C, 10x Genomics) or Visium Spatial Tissue Optimization User Guide (catalog no. CG000238 Rev C, 10x Genomics). Visium Tissue Optimization Slides were used to choose the optimal permeabilization time. For gene expression samples, tissue was permeabilized for 18 min, which was selected as the optimal time based on tissue optimization time-course experiments. Brightfield histology images of H&E stained sections were taken on a Leica Aperio CS2 slide scanner equipped with a color camera and a 20x/0.75 NA objective with a 2x optical magnification changer for 40x scanning. For tissue optimization experiments, fluorescent images were taken with a Cytation C10 Confocal Imaging Reader (Agilent) equipped with TRITC filter (ex 556/em 600) and 10x objective at approximately 400ms exposure time. Sample Br3874 contained no GCL as verified by H&E staining and incorrect spatial domain assignment by *BayesSpace* and was removed from downstream analyses.

4.3 | Visium data generation

Libraries were prepared according to the Visium Spatial Gene Expression User Guide (CG000239 Rev C, 10x Genomics). For two slides, Visium Spatial Gene Expression Slides were shipped to 10x Genomics after tissue mounting for H&E staining, and imaging, cDNA synthesis, and library preparation. Libraries were quality controlled with Agilent Bioanalyzer High Sensitivity dsDNA chips and sequenced on a NovaSeq 6000 System (Illumina) at a sequencing depth of a minimum of 60,000 reads per Visium spot. Sequencing was performed using the following read protocol: read 1: 28 cycles; i7 index read: 10 cycles; i5 index read: 10 cycles; and read 2: 90 cycles.

4.4 | Visium raw data processing

The manual alignment of raw histology images were processed by sample using 10x Genomics Loupe browser [v.6.0.0]. Raw sequencing data files (FASTQ files) for the sequenced libraries were processed using 10x Genomics Space Ranger software [v. 1.3.1], which uses human genome reference transcriptome version GRCh38 2020-A (July 7, 2020) provided by 10x Genomics for genome alignment. Software tools for performing spatial gene expression data analysis are available at: https://www.10xgenomics.com/support/spatial-gene-expression-fresh-frozen/documentation/software-analysis. The preprocessed Visium data for each sample, integrated with the output from *VistoSeg* [106] (see Methods Section 4.5, Visium H&E image segmentation and processing), were stored in a R/Bioconductor S4 class using the *SpatialExperiment* v.1.6.1 R/Bioconductor package [107].

4.5 | Visium H&E image segmentation and processing

For two Visium slides, histology images were processed and nuclei were successfully segmented using *VistoSeg*, a MATLAB-based software package [106]. Briefly, a high-resolution 40x TIFF image of the entire Visium slide is read as a RGB matrix and split in the X-direction into 4 equal matrices. The individual capture areas are saved as TIFF files at 70% resolution. Gaussian smoothing and contrast adjustment were performed to enhance the nuclei in the image. The image is converted L*a*b color space. The a*b color space is extracted from the L*a*b-converted image and is given to a K-means clustering function, along with the number of colors (k) the user visually identifies in the image. The function outputs a binary mask for each of the (k) distinguishable color gradients in the image. The segmentation is further refined by extracting the intensity of the pixels from the binary mask of nuclei and applying an intensity threshold to separate the darker nuclei regions at center from the lighter regions at the borders. Loupe Browser v.6.0.0 produces a JSON file for each

full-resolution capture area tiff from *VistoSeg*, encoding properties of the image e,g., spot diameter in pixels. Space Ranger provides a .csv file for each full-resolution capture area tiff that includes information for each spot with an identification barcode and pixel coordinates for the center of the spots. The *VistoSeg* package integrates these files with the segmented imaging data to provide a final table with nuclei count per Visium spot for each capture area/array.

4.6 | Spot-level data processing

All Visium data analyses were performed using a SpatialExperiment (*spe*) S4 class storing the object constructed with the *SpatialExperiment* v.1.6.1 R/Bioconductor package [107]. The *spe* class extends the *SingleCellExperiment* class used for scRNA-seq data for spatial context, with observations at the level of Visium spots rather than cells. Objects in the *spe* class hold additional spatial information e.g., `colData` has information on whether Visium spots overlap with the tissue from imaging data, `spatialCoords` has the *x*- and *y*-coordinates of the Visium capture areas, and `imgData` holds the imaging files and information pertaining to the images (such as pixel resolution). To the *spe* class, we added information including the sum of segmented cells per spot computed from the *VistoSeg* package, the sum of UMIs per spot, the sum of genes expressed per spot, donor age, donor sex, RNA integrity numbers (RIN), race, and post-mortem interval (PMI) hours.

Spot level analysis was performed using the same workflow as previously described [34]. Briefly, spot level quality control (QC) were evaluated using the *perCellQCMetrics* function from the *scuttle* package v.1.6.2 R Bioconductor package [108] and low quality spots having low UMI counts, low gene counts, or high percent of mitochondrial genetic expression were dropped using the *isOutlier* function of the same package. The *scran* v.1.24.0 R Bioconductor package [109] functions *quickCluster* (blocking for each brain donor) and *computeSumFactors*, then *logNormCounts* function from the *scuttle* package were used to compute the log-transformed and normalized gene expression counts at the spot level. The *scran* package functions *modelGeneVar* was used to model the gene mean expression and variance (blocking for each brain donor), and *getTopHVGs* was used to identify the top 10% HVGs. The top 10% HVGs were used to compute 50 principal components (PCs) with the runPCA function from *scater* v.1.24.0R Bioconductor package [108] and *runUMAP*, from the same package, was used for Uniform Manifold Approximation and Projection (UMAP) dimensionality reduction. Primarily for the purposes of unsupervised spatial clustering, corrections for potential batch effects and high dataset variabilities were performed by employing an transcriptomic data integration algorithm that projects Visium spots into a shared dimensionally reduced PC embedding (*Harmony* embeddings), which encourages spots to group by spot type rather than by dataset-specific conditions. The above mentioned algorithm was implemented by employing the *HarmonyMatrix* function from the *Harmony* v.0.1.0 R package [56] on a matrix containing reduced dimension coordinates for Visium spots in PC space constructed with the *reducedDim* function from the *SingleCellExperiment* v.1.18.0 R Bioconductor package [110]. This results in a QCed and batch-corrected *spe* object.

4.7 | Spatial clustering

To enable inspection of the *spe*, we generated an interactive shiny v.1.7.5 R package web application at https://libd.shinyapps.io/Lifespan_DG/ using spatialLIBD v.1.12.0 R Bioconductor package [111]. A blinded experimenter (A.R.P.) manually assigned spots to anatomical domains following consideration of marker gene expression and histological staining (**Figure S5**). Simultaneously, generation of unsupervised spatial domains were performed on the *spe* object by a separate experimenter (A.D.R.) using the *spatialCluster* function from the *BayesSpace* v.1.6.0 R Bioconductor package as previously described [57]. Briefly, the number of clusters are determined *a priori* by biological/anatomical knowledge and fixed prior to spatial clustering. For each Visium spot, a low dimensional representation of the gene expression vector is obtained from the *Harmony*

embeddings. Bayesian priors are determined by an initial non-spatial clustering with *Mclust* [112] and compared with a Markov random field given by the Potts model, which encodes information on all the spots and their neighboring spots; this allows for smoothing of initial clusters by encouraging neighboring spots to be grouped in the same cluster. The resulting Baysian model is a fixed precision matrix model, where iterative Gibbs sampling is used for updating most of the parameters in the Metropolis–Hastings algorithm; Markov chain Monte Carlo (MCMC) method is used to update latent clusters iteratively produced by the Potts model. The mode (average) of the chain for each cluster label of a spot is assigned as the final cluster label of that spot. The number of repetitions was set empirically via trial by trial basis. We chose k=10 as the number of clusters and ran *BayesSpace* at 50,000 iterations. At $k > 10$ we saw less smoothing of spatial domains and bifurcation of the GCL into two clusters with mixing of the ML. Additionally, we noted that some of the capture areas contained thalamic regions, which are enriched for inhibitory cell markers and thus included in spatial domain 6 (**Figure S6**). Since this could interfere with differential expression results pertaining to the SGZ, we set a threshold of logcount < 1 for expression of the pan-thalamic marker *TCF7L2*, which removed virtually all thalamus-containing Visium spots before pseudo-bulking and running differential expression. A total of 65,782 spots were retained for subsequent analyses. To assess cluster neighborhood purity for each Visium spot, we used the *neighborPurity* function from the *bluster* v.1.10.0 Bioconductor package, which uses a hypersphere-based approach to compute the “purity” of each cluster based on the number of contaminating spots from different clusters in its neighborhood.

4.8 | Spatial domain-level processing

For gene modeling and functional enrichment analyses, the spots were pseudo-bulked by the generated spatial domain and donor, as previously described [34]. Briefly, taking the QCed and batch-corrected *spe* object, we summed the raw gene-expression counts, for a given gene, across all spots in a given donor and a given spatial domain, and repeated this procedure for each gene with the *aggregateAcrossCells* function from the *scuttle* package. We filtered for genes that have statistically sufficiently large counts in the pseudo-bulked spatial domains with the *filterByExpr* function and calculated log normalized counts with the *calcNormFactors* function, both functions from the *edgeR* v.3.38.4 R Bioconductor package [113]. We also filtered for pseudo-bulked low Visium spot count by setting a threshold for >50 spots. Principal component analysis of the pseudo-bulked spots revealed that *BayesSpace* domain 3 had variation in many of the principal components that separated it from the other clusters, thus minimizing the variance between HPC spatial domains (**Figures S8, S10**). Examination of cluster 3 gene markers suggested that this cluster was choroid plexus (CP) (**Figure 1c)**. To prevent masking of variance within the HPC proper, *BayesSpace* domain 3 was removed from downstream analyses.

4.9 | Spatial domain-level gene modeling of age groups

Using the pseudo-bulked spatial domain-level data, spatial domains of interest were isolated or combined and the *pseudoBulkDGE* function, from the *edgeR* v.3.38.4 R Bioconductor package, was used following the limma-voom method with eBayes for differential modeling comparing one age group to all of the other age groups. We computed Student’s t-test statistics, $\log_2$FC, and adjusted p-values.

For comparing differential expression across the pseudo-bulked spatial domain-level data, gene modeling was performed using the spatialLIBD package. Briefly, the BayesSpace spatial domain labels were set as the *registration_variable*. The *registration_model* function was used to define the statistical model for computing the block correlation, with age and sex as covariates. The *registration_block_cor* function was used to compute the block correlation using the donor sample IDs as the blocking factor. Then the functions *registration_stats_enrichment*, *registration_stats_pairwise*, *registration_stats_anova* were used, employing the limma-voom method with eBayes, to fit enrichment, pairwise, and ANOVA models, respectively.

4.10 | Functional enrichment analyses

Lists of genes with adjusted *p*-values < 0.05 were compiled from pseudo-bulked spatial domains and age groups after DE analysis with *pseudoBulkDGE*. Each list of genes were computed with Over Representation Analysis (ORA) [114] to determine whether known biological functions are over-represented in each spatial domain or age group, by large gene expression differences, for the follow aspects: cellular component (intracellular locations where gene products are active, CC), molecular function (documented molecular activities associated with gene products, MF), and biological processes (sets of pathways and broader biological functions made up of the activities of multiple gene products, BP). ORA was computed with the *enrichGO* function as an argument within the *compareCluster* function from the *clusterProfiler* v.4.4.4 R Bioconductor package [115].

4.11 | Spot-level deconvolution of cell types

To perform spot-level deconvolution of cell types within Visium spots, snRNA-seq data from Franjic *et al.*, 2022 was truncated to only the DG and used as a reference dataset . We used the *cell2location* v0.1.3 Python package [64] to perform negative binomial regression to estimate reference cell type signatures. *Cell2location* establishes Baysian priors of cell abundances by using the spatial and count data from Visium, and two manually entered hyperparameters: N_cells_per_location = 5 & detection_alpha = 20. A value of 3 for N_cells_per_location is typically recommended for cortex, but, due to the cell density within the GCL, we increased the estimation. Variational Bayesian Inference is employed to produce posterior distributions of estimated cell abundances for each individual Visium spot. The mean of these distributions were then assigned to each Visium spot. Cell proportions per Visium spot were derived from the mean cell abundances per Visium spot.

4.12 | Single-molecule fluorescent in situ hybridization (smFISH/RNAscope), imaging, and analysis

Infant (n=1) and adult (n=1) hippocampal sections (10µm) were fixed in 10% neutral buffered formalin (catalog no. HT501128, Sigma-Aldrich) for 30 minutes at RT, followed by ethanol-based serial dehydration. Hybridization assays were performed according to manufacturer instructions using the RNAscope Multiplex Fluorescent Reagent Kit V2 (catalog no. 323100, Advanced Cell Diagnostics [ACD]) and the 4-plex ancillary kit V2 (catalog no. 323120, ACD). Briefly, sections were pretreated with hydrogen peroxide for 10 minutes and then permeabilized with Protease IV for 30 minutes at RT. Probes for *PROX1* (catalog no. 530241, ACD), *LAMP5* (catalog no. 487691-C2, ACD), *GAD1* (catalog no. 404031-C3, ACD), and *SLC17A7* (catalog no. 415611-C4, ACD) were applied to the slide and allowed to hybridize for 2 hours at 40 °C. Slides were washed briefly and stored in 4x saline sodium citrate (catalog no. 351–003-101, Quality Biological) overnight at 4 °C. The next day, probes were amplified and fluorescently labeled with Opal dyes as follows: PROX1 was labeled with 1:500 Opal 520 (catalog no. FP1487001KT, Akoya Biosciences [AB]), LAMP5 was labeled with 1:500 Opal 690 (catalog no. FP1497001KT, AB), GAD1 was labeled with 1:500 Opal 570 (catalog no. FP1488001KT, AB) and SLC17A7 was labeled with 1:500 Opal 620 (catalog no. FP1495001KT, AB). DAPI was applied to each slide for 20 seconds prior to mounting with Fluoromount-G (catalog no. 00-4958-02, ThermoFisher).

Slides were imaged on an AX Nikon Ti2-E confocal fluorescence microscope equipped with NIS-Elements (v5.42.02). The DG, from the ML to the CA4, was captured with a combination of tiles (30-60 tiles/image, 2048 x 2048 pixels per tile) and z-stacks (7 steps, 2µm/step, 12µm range) at 20x magnification (Nikon PLAN APO λ 20x/0.80) with a pinhole of 1.0 AU. Fluorescently-tagged probes were captured using a custom 6-channel, 3-track experiment setup that includes DAPI (405nm excitation laser, 420-500nm filter), Opal 520 (488nm

excitation laser, 500-535nm filter), Opal 570 (561nm excitation laser, 580-600nm filter), Opal 620 (561nm excitation laser, 610-630nm filter), Opal 690 (640nm excitation laser, 675-700nm filter) and a lipofuscin channel (488nm excitation laser, 700-750nm filter). All images were captured using the same laser power (LP) and gain (G) settings as follows: DAPI: 28 LP/5 G, Opal 520: 28 LP/5 G, Opal 570: 6 LP/2 G, Opal 620: 6 LP/0.5 G, Opal 690: 9 LP/1 G, Lipo: 28 LP/15 G. After capture, individual tiles were stitched together prior to max-intensity projecting. Linear unmixing was performed using Opal dye spectral standards and a human post-mortem lipofuscin spectral standard. Opal dye standards were previously created using single-positive POLR2A stained, wild-type mouse, coronal sections, where each section was stained singularly with one Opal dye (520, 570, 620, 690). After images were unmixed, they were exported as single channel .tiff files for analysis.

4.13 | Aging gene signature generation and score calculation

Computation of the common aging score (CAS) was performed similarly as previously described [55]. Using each individual pseudo-bulked spatial domain-level data to control for differences in spatial domains, the *pseudoBulkDGE* function, from the *edgeR* v.3.38.4 R Bioconductor package, was used following the limma-voom method with eBayes for differential modeling comparing each age group (teen, adult, elderly) to the infant age group. We computed Student's *t*-test statistics, log2FC, and adjusted *p*-values. Membership in the aging signature gene set was determined by being a DEG in at least two of the age-based differential modeling with thresholds of adjusted *p*-values smaller than 0.05 and a $\log_2$ fold change of at least 1.5, and shared by at least 3 spatial domains. The constructed signed gene set assigned genes with a value of 1 if positively associated with aging and -1 if negatively associated with aging. The Visium QCed count data, with no log normalization, was UMI-scaled and, along with the signed gene set, used as input for the Visium function then further processed with the analyze function from the *VISION* package v.3.0.1. Briefly, signature aging scores for every spot is calculated with the analyze function by first log-transformation and removing global cell-specific distributional effects from the signature scores by Z-normalizing the expression data, then taking the sum of expression values for positive genes minus the sum of expression values for the negative genes divided by the total amount of genes in the signed gene set. This results in a score that summaries the contrast between the positive and negative signed gene set.

To construct CAS velocities, linear modeling of CAS from age and spatial domain was performed with the lm function in R. The *lstrends* function from the *lsmeans* package v.2.30.0 with Tukey's HSD test within all possible spatial domain-to-spatial domain comparisons was used to estimate and compare the slopes of fitted lines for each spatial domain to assess significant slope differences.

Statistics and reproducibility

No statistical methods were used to predetermine sample sizes. Supplementary Table (**Table S1**) contains the demographic information for the 17 donor brains we used to generate a total of 17 section images. All box plots display the median as the center, Interquartile ranges (IQR) (25th & 75th percentiles) as the box edges, and 1.5× the IQR for the whiskers. All reported P values were two sized and were adjusted for multiple testing with Benjamini–Hochberg correction unless otherwise stated. Distributions of the residuals of the linear modeling were assumed to be normally distributed across all genes and models, but this was not formally tested. Wilcoxon signed-rank test used for comparing mean cell abundances between two age groups. Tukey's HSD test was used across all possible spatial domain-to-spatial domain comparisons of CAS slopes. Visium spots that were outside of tissue or did not pass QC checks were omitted from all analyses. We used the brain donors as a blocking factor in our analyses, as they were also unique for each Visium capture area. Data collection and analysis were not performed blind to the conditions of the experiments. Plots in R were created either in base R or with the *ggplot2* R package [116]. Figures were compiled with the help of BioRender.com.

Additional resources

To visualize the spot-level Visium data and as a resource to the neuroscience community, we created a shiny [117] interactive browser available at https://libd.shinyapps.io/Lifespan_DG/ which is powered by the *spatialLIBD* v.1.8.11 R Bioconductor package [111].

4.14 | Data Availability

The raw and processed data are publicly available through Zenodo listed at https://doi.org/10.5281/zenodo.10126688 [118]. The raw data provided through Zenodo include all the FASTQ files and raw image files. The processed data include two *spe* objects: (1) with the untransformed feature counts, and (2) with normalized $\log_2$ transformed feature counts, batch correction, unsupervised spatial clustering, and cell-type deconvolution.

4.15 | Code Availability

The code for this project is publicly available through GitHub at https://github.com/LieberInstitute/spatial_DG_lifespan [119] and is described in the associated README.md file. Analyses were performed using R v.4.2.1 with Bioconductor v.3.15.2. *cell2location* v0.1.3 was employed via *reticulate* R package v.1.28.

4.16 | Acknowledgements, Funding, Authorship Contributions

We thank the LIBD neuropathology team, particularly James Tooke and Amy Deep-Soboslay, for curation of the brain samples and assistance with tissue dissections. We thank the staff and physicians at the brain donation sites, and the generosity of the brain donors and their families, without whom this work would not be possible. We thank Andrew E Jaffe, Daniel R Weinberger, and members of the LIBD spatial team for helpful feedback to the manuscript. Finally, we thank the families of Connie and Steve Lieber and Milton and Tamar Maltz for their generous support.

Funding for this project was provided by U01MH122849 (KM), R21AG083328 (SCP and SCH), and the Lieber Institute for Brain Development.

Authorship Contributions:
Conceptualization: ADR, KM, SCP
Data Curation: ADR, HRD, SCP
Formal Analysis: ADR, MT, HRD, SCH
Investigation: ADR, HRD, ARP, EAP, SCP
Methodology: ADR, SCH
Validation: ADR, ARP
Resources: JEK, TRH
Software: ADR, HRD, RAM
Visualization: ADR, ARP
Project Administration: KRM, LC-T, KM, SCH, SCP
Supervision: KRM, KM, SCH, SCP
Funding acquisition: KM, SCH, SCP
Writing – original draft: ADR
Writing – review & editing: ADR, KM, SCH, SCP

Author ORCID:
Anthony D. Ramnauth[1,2], https://orcid.org/0000-0001-5373-0857

Madhavi Tippani[1], https://orcid.org/0000-0002-6465-6418
Heena R. Divecha[1], https://orcid.org/0000-0002-1959-0675
Alexis R. Papariello[1], https://orcid.org/0000-0001-6746-5054
Ryan A. Miller[1], https://orcid.org/0000-0003-3477-7443
Elizabeth A. Pattie[1], https://orcid.org/0009-0009-5729-4971
Joel E. Kleinman[1,3],
Kristen R. Maynard[1,2,3], https://orcid.org/0000-0003-0031-8468
Leonardo Collado-Torres[1,4], https://orcid.org/0000-0003-2140-308X
Thomas M. Hyde[1,3,5], https://orcid.org/0000-0002-8746-3037
Keri Martinowich[1,2,3,6,+] , https://orcid.org/0000-0002-5237-0789
Stephanie C. Hicks[4,7,8,9,+], https://orcid.org/0000-0002-7858-0231
Stephanie C. Page[1,+] https://orcid.org/0000-0002-1951-7398

5 | Supplementary Materials

5.1 | Supplementary Tables

Supplementary Table 1
Demographic information on brain donors, including information on brain id # (BrNum), age of death, slide and capture area for each Visium slide, sex, ancestry, RIN for PFC tissue (Screening RIN PFC, performed at time of collection), post mortem interval (PMI), and psychiatric diagnoses (PrimaryDx).

Supplementary Table 2
Manual annotations across all Visium spots from scientist blinded to experiments. Contains information on donor tissue sample (sample_id), spatial barcode (spot_name), and manual annotation.

Supplementary Table 3
DEGs across aggregated DG spatial domains for each age group vs. all others. Contains information on ENSEMBL gene id (gene_id), gene name (gene_name), protein coding or not (gene_type), p-value, adjusted p-value, and $\log_2$ fold-change.

Supplementary Table 4
All significant upregulated/downregulated GO terms from DG age groups vs. all others. Contains information on age group (Cluster), upregulated or downregulated, accession ID (ID), GO term description, ratio of genes from gene set in GO term (GeneRatio), ratio of genes from all genes (BgRatio), p-value, adjusted p-value, q-values, list of genes in GO term (geneID), and number of genes from gene set in GO term (Count).

Supplementary Table 5
DEGs from age groups vs. all others for each separate DG spatial domain and the SLM. Contains information on ENSEMBL gene id (gene_id), gene name (gene_name), protein coding or not (gene_type), p-value, adjusted p-value, and $\log_2$ fold-change.

Supplementary Table 6

Signed gene set that makes up the common HPC aging signature. Contains information on ENSEMBL gene id (gene_id), gene name (gene_name), protein coding or not (gene_type), and sign for positively associated aging genes or negatively associated aging genes.

References

1. Lavenex, P. & Banta Lavenex, P. Building hippocampal circuits to learn and remember: insights into the development of human memory. *Behav. Brain Res.* **254**, 8–21 (2013).
2. Ghetti, S. & Bunge, S. A. Neural changes underlying the development of episodic memory during middle childhood. *Dev. Cogn. Neurosci.* **2**, 381–395 (2012).
3. Petersen, R. C. Mild Cognitive Impairment. *Continuum (Minneap Minn)* **22**, 404–418 (2016).
4. Plassman, B. L. *et al.* Prevalence of cognitive impairment without dementia in the United States. *Ann. Intern. Med.* **148**, 427–434 (2008).
5. Boyle, P. A. *et al.* Much of late life cognitive decline is not due to common neurodegenerative pathologies. *Ann. Neurol.* **74**, 478–489 (2013).
6. Watson, R., Colloby, S. J., Blamire, A. M. & O'Brien, J. T. Subcortical volume changes in dementia with Lewy bodies and Alzheimer's disease. A comparison with healthy aging. *Int. Psychogeriatr.* **28**, 529–536 (2016).
7. Dickerson, B. C. *et al.* Increased hippocampal activation in mild cognitive impairment compared to normal aging and AD. *Neurology* **65**, 404–411 (2005).
8. Hainmueller, T. & Bartos, M. Dentate gyrus circuits for encoding, retrieval and discrimination of episodic memories. *Nat. Rev. Neurosci.* **21**, 153–168 (2020).
9. Kesner, R. P. An analysis of dentate gyrus function (an update). *Behav. Brain Res.* **354**, 84–91 (2018).
10. Xavier, G. F. & Costa, V. C. I. Dentate gyrus and spatial behaviour. *Prog Neuropsychopharmacol Biol Psychiatry* **33**, 762–773 (2009).
11. Zou, D. *et al.* DREADD in parvalbumin interneurons of the dentate gyrus modulates anxiety, social interaction and memory extinction. *Curr. Mol. Med.* **16**, 91–102 (2016).
12. Chen, S. *et al.* Defects of parvalbumin-positive interneurons in the ventral dentate gyrus region are implicated depression-like behavior in mice. *Brain Behav. Immun.* **99**, 27–42 (2022).
13. Karayol, R. *et al.* Serotonin receptor 4 in the hippocampus modulates mood and anxiety. *Mol. Psychiatry* **26**, 2334–2349 (2021).

14. Amaral, D. G., Scharfman, H. E. & Lavenex, P. The dentate gyrus: fundamental neuroanatomical organization (dentate gyrus for dummies). *Prog. Brain Res.* **163**, 3–22 (2007).

15. Seress, L. Comparative anatomy of the hippocampal dentate gyrus in adult and developing rodents, non-human primates and humans. in *The Dentate Gyrus: A Comprehensive Guide to Structure, Function, and Clinical Implications* vol. 163 23–798 (Elsevier, 2007).

16. Strange, B. A., Witter, M. P., Lein, E. S. & Moser, E. I. Functional organization of the hippocampal longitudinal axis. *Nat. Rev. Neurosci.* **15**, 655–669 (2014).

17. Snyder, J. S. Recalibrating the relevance of adult neurogenesis. *Trends Neurosci.* **42**, 164–178 (2019).

18. Hochgerner, H., Zeisel, A., Lönnerberg, P. & Linnarsson, S. Conserved properties of dentate gyrus neurogenesis across postnatal development revealed by single-cell RNA sequencing. *Nat. Neurosci.* **21**, 290–299 (2018).

19. Hao, Z.-Z. *et al.* Single-cell transcriptomics of adult macaque hippocampus reveals neural precursor cell populations. *Nat. Neurosci.* **25**, 805–817 (2022).

20. Eriksson, P. S. *et al.* Neurogenesis in the adult human hippocampus. *Nat. Med.* **4**, 1313–1317 (1998).

21. Knoth, R. *et al.* Murine features of neurogenesis in the human hippocampus across the lifespan from 0 to 100 years. *PLoS ONE* **5**, e8809 (2010).

22. Dennis, C. V., Suh, L. S., Rodriguez, M. L., Kril, J. J. & Sutherland, G. T. Human adult neurogenesis across the ages: An immunohistochemical study. *Neuropathol. Appl. Neurobiol.* **42**, 621–638 (2016).

23. Boldrini, M. *et al.* Human Hippocampal Neurogenesis Persists throughout Aging. *Cell Stem Cell* **22**, 589-599.e5 (2018).

24. Moreno-Jiménez, E. P. *et al.* Adult hippocampal neurogenesis is abundant in neurologically healthy subjects and drops sharply in patients with Alzheimer's disease. *Nature Medicine* (2019).

25. Tobin, M. K. *et al.* Human hippocampal neurogenesis persists in aged adults and alzheimer's disease patients. *Cell Stem Cell* **24**, 974-982.e3 (2019).

26. Seki, T., Hori, T., Miyata, H., Maehara, M. & Namba, T. Analysis of proliferating neuronal progenitors and immature neurons in the human hippocampus surgically removed from control and epileptic patients. *Sci. Rep.* **9**, 18194 (2019).

27. Terreros-Roncal, J. *et al.* Impact of neurodegenerative diseases on human adult hippocampal

neurogenesis. *Science* **374**, 1106–1113 (2021).

28. Ammothumkandy, A. *et al.* Altered adult neurogenesis and gliogenesis in patients with mesial temporal lobe epilepsy. *Nat. Neurosci.* **25**, 493–503 (2022).

29. Franjic, D. *et al.* Transcriptomic taxonomy and neurogenic trajectories of adult human, macaque, and pig hippocampal and entorhinal cells. *Neuron* **110**, 452-469.e14 (2022).

30. Ayhan, F. *et al.* Resolving cellular and molecular diversity along the hippocampal anterior-to-posterior axis in humans. *Neuron* **109**, 2091-2105.e6 (2021).

31. Hafner, A.-S., Donlin-Asp, P. G., Leitch, B., Herzog, E. & Schuman, E. M. Local protein synthesis is a ubiquitous feature of neuronal pre- and postsynaptic compartments. *Science* **364**, (2019).

32. Stickels, R. R. *et al.* Highly sensitive spatial transcriptomics at near-cellular resolution with Slide-seqV2. *Nat. Biotechnol.* **39**, 313–319 (2021).

33. Niu, M. *et al.* Droplet-based transcriptome profiling of individual synapses. *Nat. Biotechnol.* (2023) doi:10.1038/s41587-022-01635-1.

34. Maynard, K. R. *et al.* Transcriptome-scale spatial gene expression in the human dorsolateral prefrontal cortex. *Nat. Neurosci.* **24**, 425–436 (2021).

35. Collado-Torres, L. *et al.* Regional Heterogeneity in Gene Expression, Regulation, and Coherence in the Frontal Cortex and Hippocampus across Development and Schizophrenia. *Neuron* **103**, 203-216.e8 (2019).

36. Jaffe, A. E. *et al.* Profiling gene expression in the human dentate gyrus granule cell layer reveals insights into schizophrenia and its genetic risk. *Nat. Neurosci.* **23**, 510–519 (2020).

37. Josselyn, S. A. & Frankland, P. W. Infantile amnesia: a neurogenic hypothesis. *Learn. Mem.* **19**, 423–433 (2012).

38. Gao, A. *et al.* Elevation of hippocampal neurogenesis induces a temporally graded pattern of forgetting of contextual fear memories. *J. Neurosci.* **38**, 3190–3198 (2018).

39. Tran, L. M., Josselyn, S. A., Richards, B. A. & Frankland, P. W. Forgetting at biologically realistic levels of neurogenesis in a large-scale hippocampal model. *Behav. Brain Res.* **376**, 112180 (2019).

40. Scott, G. A. *et al.* Adult neurogenesis mediates forgetting of multiple types of memory in the rat. *Mol. Brain* **14**, 97 (2021).

41. Akers, K. G. *et al.* Hippocampal neurogenesis regulates forgetting during adulthood and infancy. *Science* **344**, 598–602 (2014).

42. Montagne, A. *et al.* Blood-brain barrier breakdown in the aging human hippocampus. *Neuron* **85**, 296–302 (2015).

43. Jin, W.-N. *et al.* Neuroblast senescence in the aged brain augments natural killer cell cytotoxicity leading to impaired neurogenesis and cognition. *Nat. Neurosci.* **24**, 61–73 (2021).

44. Menet, V., Ribotta, M. G. Y., Sandillon, F. & Privat, A. GFAP null astrocytes are a favorable substrate for neuronal survival and neurite growth. *Glia* (2000).

45. Larsson, A., Wilhelmsson, U., Pekna, M. & Pekny, M. Increased cell proliferation and neurogenesis in the hippocampal dentate gyrus of old GFAP(-/-)Vim(-/-) mice. *Neurochem. Res.* **29**, 2069–2073 (2004).

46. Barrientos, R. M., Kitt, M. M., Watkins, L. R. & Maier, S. F. Neuroinflammation in the normal aging hippocampus. *Neuroscience* **309**, 84–99 (2015).

47. Liddelow, S. A. *et al.* Neurotoxic reactive astrocytes are induced by activated microglia. *Nature* **541**, 481–487 (2017).

48. Clarke, L. E. *et al.* Normal aging induces A1-like astrocyte reactivity. *Proc Natl Acad Sci USA* **115**, E1896–E1905 (2018).

49. Mathys, H. *et al.* Temporal Tracking of Microglia Activation in Neurodegeneration at Single-Cell Resolution. *Cell Rep.* **21**, 366–380 (2017).

50. Maciel-Barón, L. Á. *et al.* Cellular senescence, neurological function, and redox state. *Antioxid. Redox Signal.* **28**, 1704–1723 (2018).

51. Angelova, D. M. & Brown, D. R. Microglia and the aging brain: are senescent microglia the key to neurodegeneration? *J. Neurochem.* **151**, 676–688 (2019).

52. Neumann, P., Lenz, D. E., Streit, W. J. & Bechmann, I. Is microglial dystrophy a form of cellular senescence? An analysis of senescence markers in the aged human brain. *Glia* **71**, 377–390 (2023).

53. Lana, D., Ugolini, F., Nosi, D., Wenk, G. L. & Giovannini, M. G. The emerging role of the interplay among astrocytes, microglia, and neurons in the hippocampus in health and disease. *Front. Aging Neurosci.* **13**, 651973 (2021).

54. Galatro, T. F. *et al.* Transcriptomic analysis of purified human cortical microglia reveals age-associated

changes. *Nat. Neurosci.* **20**, 1162–1171 (2017).

55. Hahn, O. *et al.* Atlas of the aging mouse brain reveals white matter as vulnerable foci. *Cell* **186**, 4117-4133.e22 (2023).

56. Korsunsky, I. *et al.* Fast, sensitive and accurate integration of single-cell data with Harmony. *Nat. Methods* **16**, 1289–1296 (2019).

57. Zhao, E. *et al.* Spatial transcriptomics at subspot resolution with BayesSpace. *Nat. Biotechnol.* **39**, 1375–1384 (2021).

58. Lun, A. bluster: Clustering Algorithms for Bioconductor. R package version 1.8.0. *Bioconductor* (2022) doi:10.18129/b9.bioc.bluster.

59. Huang, T.-T., Zou, Y. & Corniola, R. Oxidative stress and adult neurogenesis--effects of radiation and superoxide dismutase deficiency. *Semin. Cell Dev. Biol.* **23**, 738–744 (2012).

60. Aguilar-Hernández, L., Alejandre, R., César Morales-Medina, J., Iannitti, T. & Flores, G. Cellular mechanisms in brain aging: Focus on physiological and pathological aging. *J. Chem. Neuroanat.* **128**, 102210 (2023).

61. Mattson, M. P. & Arumugam, T. V. Hallmarks of brain aging: adaptive and pathological modification by metabolic states. *Cell Metab.* **27**, 1176–1199 (2018).

62. Troubat, R. *et al.* Neuroinflammation and depression: A review. *Eur. J. Neurosci.* **53**, 151–171 (2021).

63. Bettio, L. E. B., Rajendran, L. & Gil-Mohapel, J. The effects of aging in the hippocampus and cognitive decline. *Neurosci. Biobehav. Rev.* **79**, 66–86 (2017).

64. Kleshchevnikov, V. *et al.* Cell2location maps fine-grained cell types in spatial transcriptomics. *Nat. Biotechnol.* **40**, 661–671 (2022).

65. Li, H. *et al.* A comprehensive benchmarking with practical guidelines for cellular deconvolution of spatial transcriptomics. *Nat. Commun.* **14**, 1548 (2023).

66. Ma, S.-M. *et al.* Periostin Promotes Neural Stem Cell Proliferation and Differentiation following Hypoxic-Ischemic Injury. *PLoS ONE* **10**, e0123585 (2015).

67. Zhou, Y. *et al.* Molecular landscapes of human hippocampal immature neurons across lifespan. *Nature* **607**, 527–533 (2022).

68. DeTomaso, D. *et al.* Functional interpretation of single cell similarity maps. *Nat. Commun.* **10**, 4376

(2019).

69. Marioni, R. E. *et al.* DNA methylation age of blood predicts all-cause mortality in later life. *Genome Biol.* **16**, 1–12 (2015).

70. Nishiyama, A., Shimizu, T., Sherafat, A. & Richardson, W. D. Life-long oligodendrocyte development and plasticity. *Semin. Cell Dev. Biol.* **116**, 25–37 (2021).

71. Dutta, S. & Sengupta, P. Men and mice: Relating their ages. *Life Sci.* **152**, 244–248 (2016).

72. Wang, S., Lai, X., Deng, Y. & Song, Y. Correlation between mouse age and human age in anti-tumor research: Significance and method establishment. *Life Sci.* **242**, 117242 (2020).

73. Su, Y. *et al.* A single-cell transcriptome atlas of glial diversity in the human hippocampus across the postnatal lifespan. *Cell Stem Cell* **29**, 1594-1610.e8 (2022).

74. Urrutia, P. *et al.* Inflammation alters the expression of DMT1, FPN1 and hepcidin, and it causes iron accumulation in central nervous system cells. *J. Neurochem.* **126**, 541–549 (2013).

75. Srpan, K. *et al.* Shedding of CD16 disassembles the NK cell immune synapse and boosts serial engagement of target cells. *J. Cell Biol.* **217**, 3267–3283 (2018).

76. Warren, H. S. & Kinnear, B. F. Quantitative analysis of the effect of CD16 ligation on human NK cell proliferation. *J. Immunol.* **162**, 735–742 (1999).

77. Sierksma, A. *et al.* Novel Alzheimer risk genes determine the microglia response to amyloid-β but not to TAU pathology. *EMBO Mol. Med.* **12**, e10606 (2020).

78. Mukherjee, S., Klaus, C., Pricop-Jeckstadt, M., Miller, J. A. & Struebing, F. L. A Microglial Signature Directing Human Aging and Neurodegeneration-Related Gene Networks. *Front. Neurosci.* **13**, 2 (2019).

79. Liu, J. *et al.* Expression and regulatory characteristics of peripheral blood immune cells in primary Sjögren's syndrome patients using single-cell transcriptomic. *iScience* **25**, 105509 (2022).

80. Gingrich, A. A. *et al.* Cross-species gene expression analysis of human, canine and murine natural killer cells suggests convergence of activated dog and human transcriptomic profiles. *The Journal of Immunology* **204**, 92.24-92.24 (2020).

81. Dulken, B. W. *et al.* Single-cell analysis reveals T cell infiltration in old neurogenic niches. *Nature* **571**, 205–210 (2019).

82. Radjavi, A., Smirnov, I., Derecki, N. & Kipnis, J. Dynamics of the meningeal CD4(+) T-cell repertoire are

defined by the cervical lymph nodes and facilitate cognitive task performance in mice. *Mol. Psychiatry* **19**, 531–533 (2014).

83. Ziv, Y. *et al.* Immune cells contribute to the maintenance of neurogenesis and spatial learning abilities in adulthood. *Nat. Neurosci.* **9**, 268–275 (2006).

84. Kim, H. *et al.* Reactive astrocytes transduce inflammation in a blood-brain barrier model through a TNF-STAT3 signaling axis and secretion of alpha 1-antichymotrypsin. *Nat. Commun.* **13**, 6581 (2022).

85. Denisenko, E. *et al.* Systematic assessment of tissue dissociation and storage biases in single-cell and single-nucleus RNA-seq workflows. *Genome Biol.* **21**, 130 (2020).

86. van den Brink, S. C. *et al.* Single-cell sequencing reveals dissociation-induced gene expression in tissue subpopulations. *Nat. Methods* **14**, 935–936 (2017).

87. Romero-Santacreu, L., Moreno, J., Pérez-Ortín, J. E. & Alepuz, P. Specific and global regulation of mRNA stability during osmotic stress in Saccharomyces cerevisiae. *RNA* **15**, 1110–1120 (2009).

88. Xiong, L., Lee, H., Ishitani, M. & Zhu, J.-K. Regulation of osmotic stress-responsive gene expression by the LOS6/ABA1 locus in Arabidopsis. *J. Biol. Chem.* **277**, 8588–8596 (2002).

89. Maynard, K. R. *et al.* dotdotdot: an automated approach to quantify multiplex single molecule fluorescent in situ hybridization (smFISH) images in complex tissues. *Nucleic Acids Res.* (2020) doi:10.1093/nar/gkaa312.

90. Lein, E., Borm, L. E. & Linnarsson, S. The promise of spatial transcriptomics for neuroscience in the era of molecular cell typing. *Science* **358**, 64–69 (2017).

91. Crosetto, N., Bienko, M. & van Oudenaarden, A. Spatially resolved transcriptomics and beyond. *Nat. Rev. Genet.* **16**, 57–66 (2015).

92. Tiveron, M.-C. *et al.* LAMP5 Fine-Tunes GABAergic Synaptic Transmission in Defined Circuits of the Mouse Brain. *PLoS ONE* **11**, e0157052 (2016).

93. Lee, B. R. *et al.* Signature morphoelectric properties of diverse GABAergic interneurons in the human neocortex. *Science* **382**, eadf6484 (2023).

94. Yu, B. *et al.* Molecular and cellular evolution of the amygdala across species analyzed by single-nucleus transcriptome profiling. *Cell Discov.* **9**, 19 (2023).

95. Hodge, R. D. *et al.* Conserved cell types with divergent features in human versus mouse cortex. *Nature*

573, 61–68 (2019).

96. Deng, Y. *et al.* Loss of LAMP5 interneurons drives neuronal network dysfunction in Alzheimer's disease. *Acta Neuropathol.* **144**, 637–650 (2022).

97. Chen, W. *et al.* Cross-Species Analysis of Gene Expression and Function in Prefrontal Cortex, Hippocampus and Striatum. *PLoS ONE* **11**, e0164295 (2016).

98. Diep, D. B., Hoen, N., Backman, M., Machon, O. & Krauss, S. Characterisation of the Wnt antagonists and their response to conditionally activated Wnt signalling in the developing mouse forebrain. *Brain Res. Dev. Brain Res.* **153**, 261–270 (2004).

99. Griñan-Ferré, C. *et al.* Environmental Enrichment Improves Behavior, Cognition, and Brain Functional Markers in Young Senescence-Accelerated Prone Mice (SAMP8). *Mol. Neurobiol.* **53**, 2435–2450 (2016).

100. Li, H. *et al.* Pleiotrophin ameliorates age-induced adult hippocampal neurogenesis decline and cognitive dysfunction. *Cell Rep.* **42**, 113022 (2023).

101. Ramsaran, A. I. *et al.* A shift in the mechanisms controlling hippocampal engram formation during brain maturation. *Science* **380**, 543–551 (2023).

102. Bryan, K. J. *et al.* Expression of CD74 is increased in neurofibrillary tangles in Alzheimer's disease. *Mol. Neurodegener.* **3**, 13 (2008).

103. Kiyota, T. *et al.* AAV2/1 CD74 Gene Transfer Reduces β-amyloidosis and Improves Learning and Memory in a Mouse Model of Alzheimer's Disease. *Mol. Ther.* **23**, 1712–1721 (2015).

104. Matsuda, S., Matsuda, Y. & D'Adamio, L. CD74 interacts with APP and suppresses the production of Abeta. *Mol. Neurodegener.* **4**, 41 (2009).

105. Lipska, B. K. *et al.* Critical factors in gene expression in postmortem human brain: Focus on studies in schizophrenia. *Biol. Psychiatry* **60**, 650–658 (2006).

106. Tippani, M. *et al. VistoSeg* : processing utilities for high resolution images for spatially resolved transcriptomics data. *Biol. Imaging* 1–21 (2023) doi:10.1017/S2633903X23000235.

107. Righelli, D. *et al.* SpatialExperiment: infrastructure for spatially-resolved transcriptomics data in R using Bioconductor. *Bioinformatics* **38**, 3128–3131 (2022).

108. McCarthy, D. J., Campbell, K. R., Lun, A. T. L. & Wills, Q. F. Scater: pre-processing, quality control,

normalization and visualization of single-cell RNA-seq data in R. *Bioinformatics* **33**, 1179–1186 (2017).

109. Lun, A. T. L., McCarthy, D. J. & Marioni, J. C. A step-by-step workflow for low-level analysis of single-cell RNA-seq data with Bioconductor. [version 2; peer review: 3 approved, 2 approved with reservations]. *F1000Res.* **5**, 2122 (2016).

110. Amezquita, R. A. *et al.* Orchestrating single-cell analysis with Bioconductor. *Nat. Methods* **17**, 137–145 (2020).

111. Pardo, B. *et al.* spatialLIBD: an R/Bioconductor package to visualize spatially-resolved transcriptomics data. *BMC Genomics* **23**, 434 (2022).

112. Scrucca, L., Fop, M., Murphy, T. B. & Raftery, A. E. mclust 5: Clustering, Classification and Density Estimation Using Gaussian Finite Mixture Models. *R J.* **8**, 289–317 (2016).

113. Robinson, M. D., McCarthy, D. J. & Smyth, G. K. edgeR: a Bioconductor package for differential expression analysis of digital gene expression data. *Bioinformatics* **26**, 139–140 (2010).

114. Boyle, E. I. *et al.* GO::TermFinder--open source software for accessing Gene Ontology information and finding significantly enriched Gene Ontology terms associated with a list of genes. *Bioinformatics* **20**, 3710–3715 (2004).

115. Wu, T. *et al.* clusterProfiler 4.0: A universal enrichment tool for interpreting omics data. *Innovation (Camb)* **2**, 100141 (2021).

116. Wickham, H. *ggplot2 - Elegant Graphics for Data Analysis*. (Springer International Publishing, 2016). doi:10.1007/978-3-319-24277-4.

117. Chang, W., Cheng, J., Allaire, J. J., Xie, Y. & McPherson, J. shiny: Web Application Framework for R. (2019).

118. Miller, R., Page, S. & Anthony, R. LieberInstitute/spatial_DG_lifespan: v1.0.0. *Zenodo* (2023) doi:10.5281/zenodo.10126688.

119. LieberInstitute/spatial_DG_lifespan: LieberInstitute/spatial_DG_lifespan: v1.0.0. *Zenodo* (2023) doi:10.5281/zenodo.10126716.

6 | Main Figures and Legends

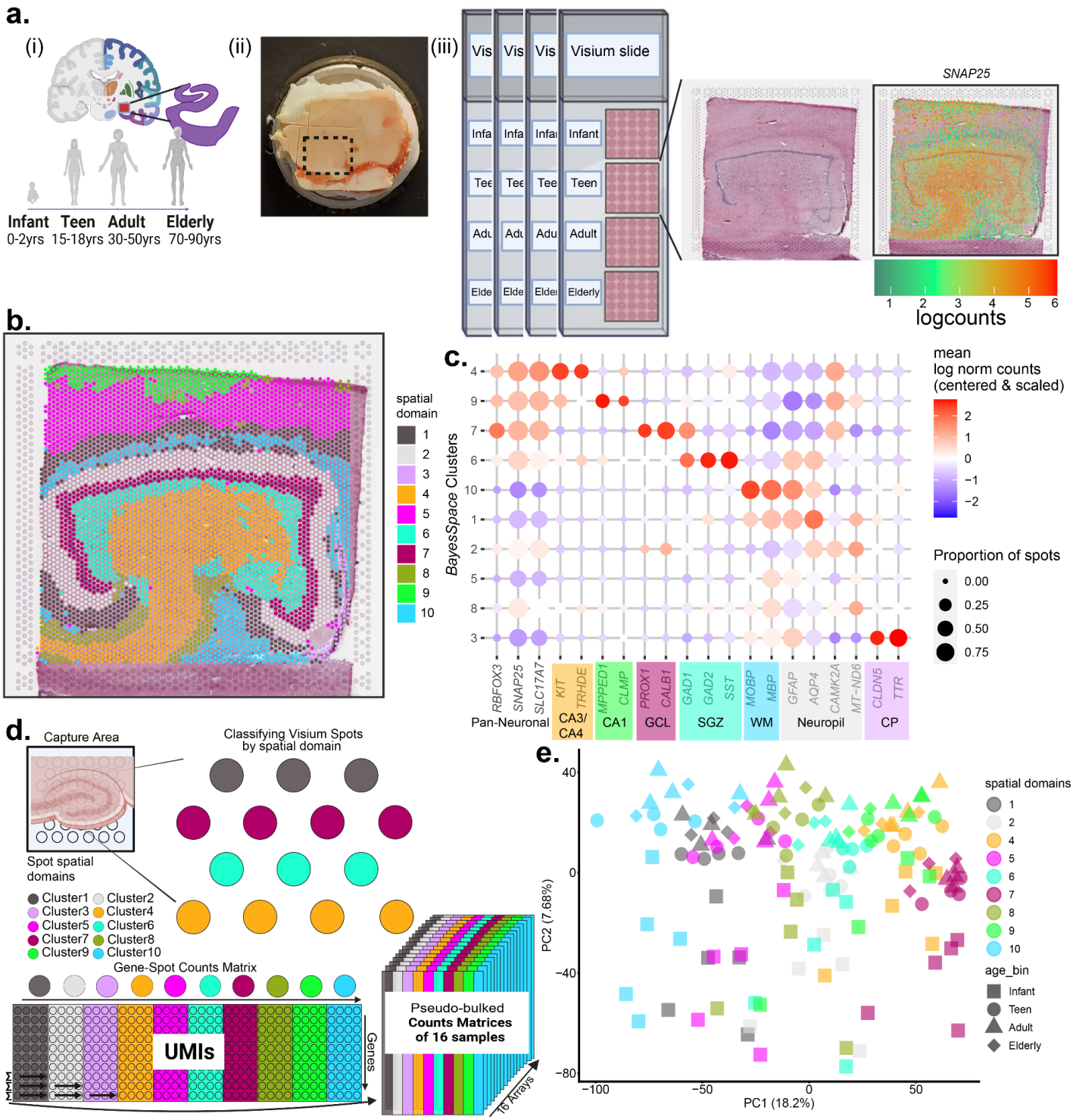

Figure 1: Spatially-resolved transcriptomic profiling and unsupervised spatial domain detection in the human dentate gyrus across the postnatal lifespan. (a) (i) Schematic of experimental design to molecularly profile the human dentate gyrus (DG) from four age groups: infant (0-2 years), teen (13-18 years), adult (30-50 years), and elderly (70+ years). (ii) Tissue blocks were dissected from frozen brain slabs and scored to isolate the DG, then (iii) cryosectioned at 10µm, mounted onto 10x Genomics Visium slides, and stained using hematoxylin and eosin (H&E) to visualize tissue morphology. (iv) On-slide cDNA synthesis was performed, followed by library construction and Illumina sequencing, resulting in spatially barcoded transcript counts as illustrated by *SNAP25* expression. **(b)** Example spot plot of a capture area from donor Br1412 covering the DG where Visium spots are labeled by the *BayesSpace* spatial domain detection algorithm (k=10). **(c)** Dot plot for canonical spatial domain-specific and neuropil-enriched gene markers averaged across gene (columns) for 10 domains (rows). Dots are sized by the proportion of spots with nonzero expression and colored by mean $\log_2$ normalized counts, centered and scaled. (**d**) Illustration of pseudo-bulking spots across predicted spatial domains for each of the

N=16 capture areas. **(e)** Scatter plot of the first two principal components (PCs) after pseudo-bulking spots for each capture area and spatial domain (excluding cluster 3) colored by spatial domain and shaped by age bin, with percent variance explained in parentheses.

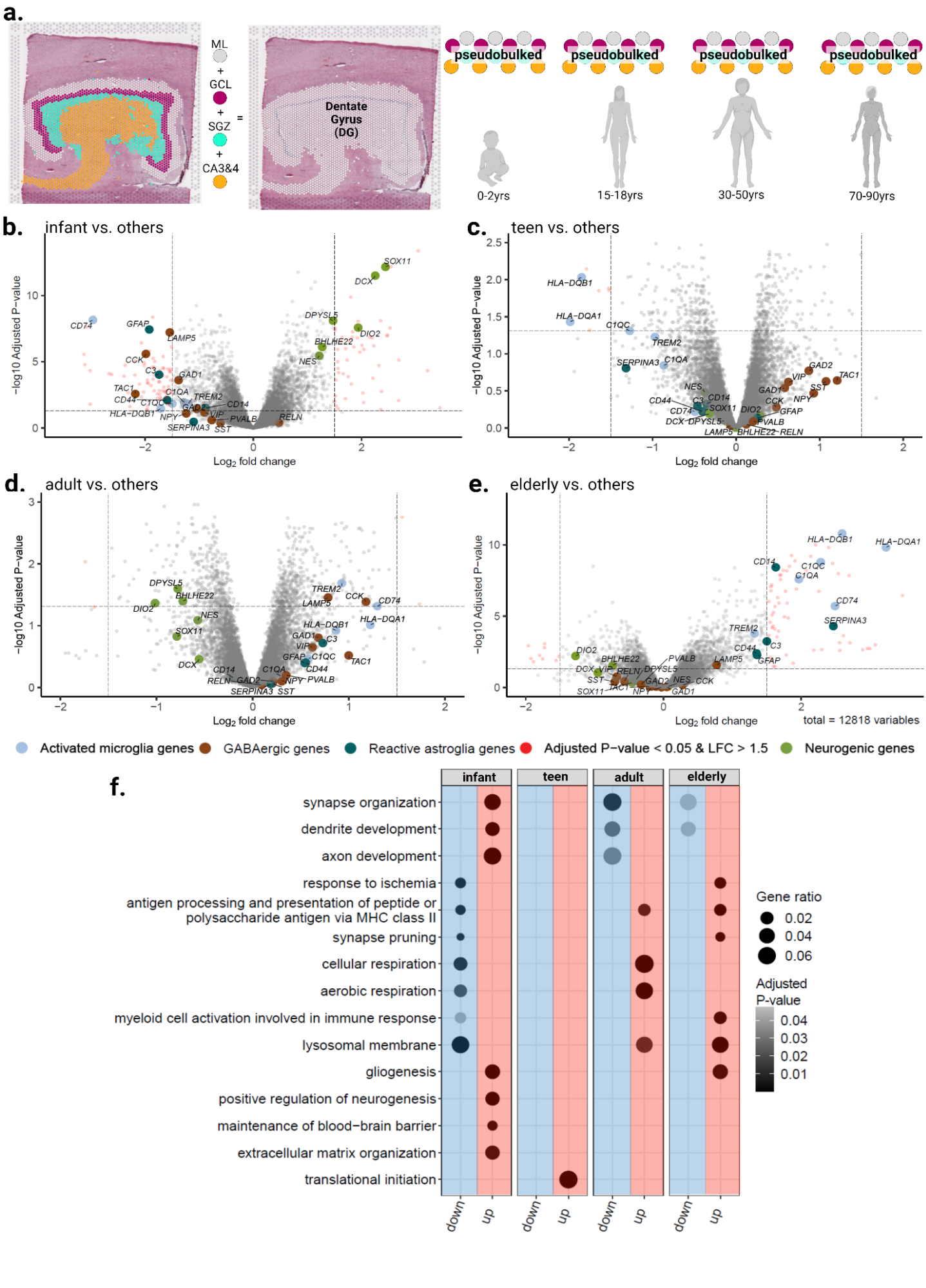

Figure 2. Differential expression analysis composite DG identifies genes associated with specific lifespan stages (infant, teen, adult, elderly). (**a**) Predicted spatial domains (ML, GCL, SGZ and CA3&4) were collapsed and pseudo-bulked to generate molecular profiles representing the composite DG region for each donor. (**b-e**) Volcano plots after performing differential expression using pseudo-bulked DG samples, comparing one age group to all others. Point colors highlight select genes associated with major hallmarks of aging such as neurogenesis (green), activated microglia (light blue), and reactive astroglia (dark green). The *x*-axis is the $\log_2$ fold change in expression highlighting genes ≥1.5 logFC or ≤-1.5 logFC and the *y*-axis is the negative $\log_{10}$ adjusted *p*-values (*y*-axis range varies across four plots). (**f**) Dot plots for major gene ontology terms. Dot plots are faceted by age groups with their down- and up-regulation columns colored by blue and red, respectively; dot size represents the fraction of gene set that was differentially expressed (Gene ratio), while black gradient represents adjusted *p*-value.

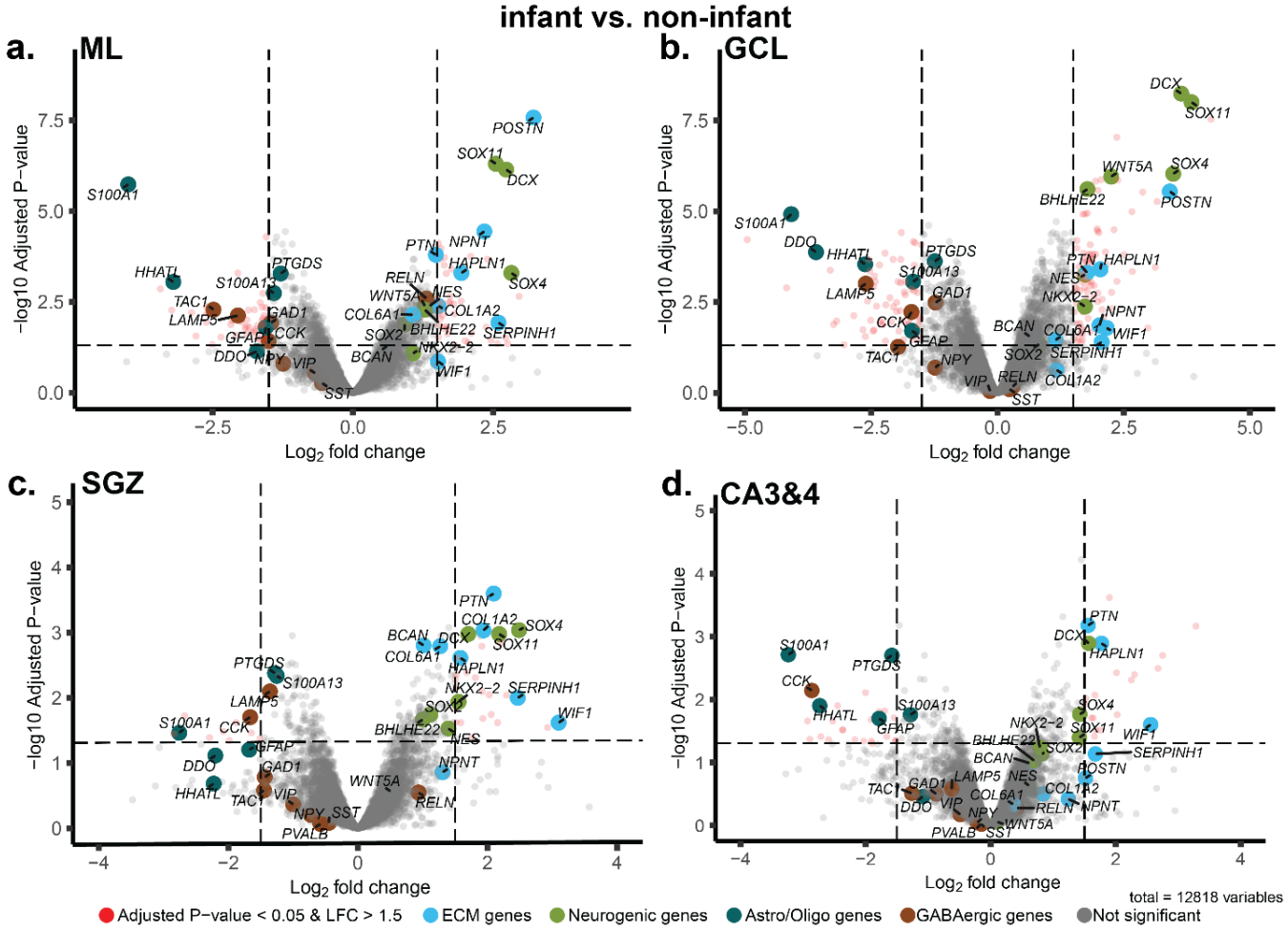

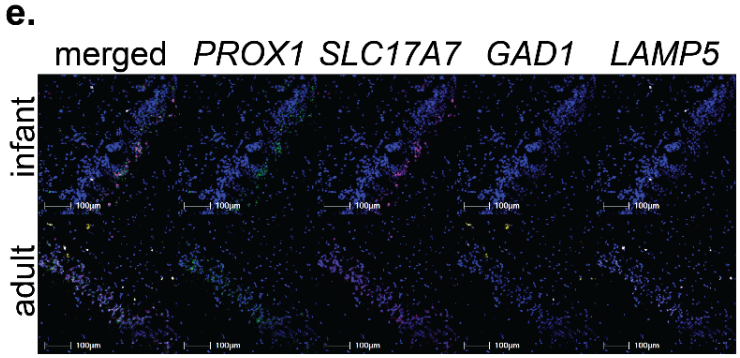

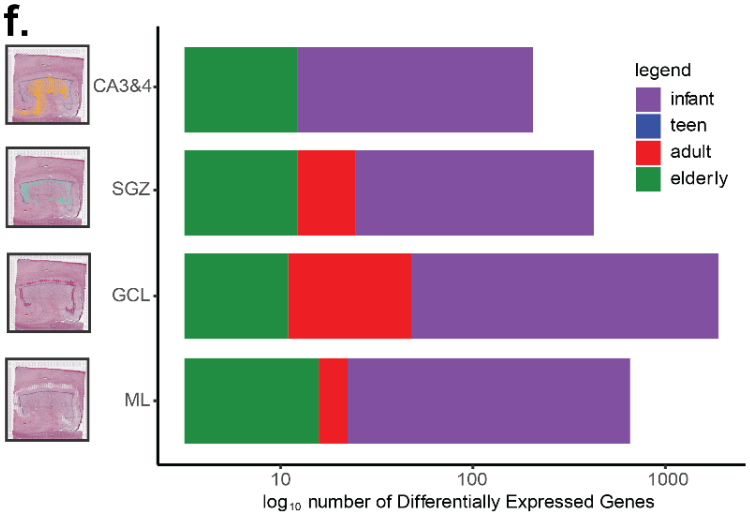

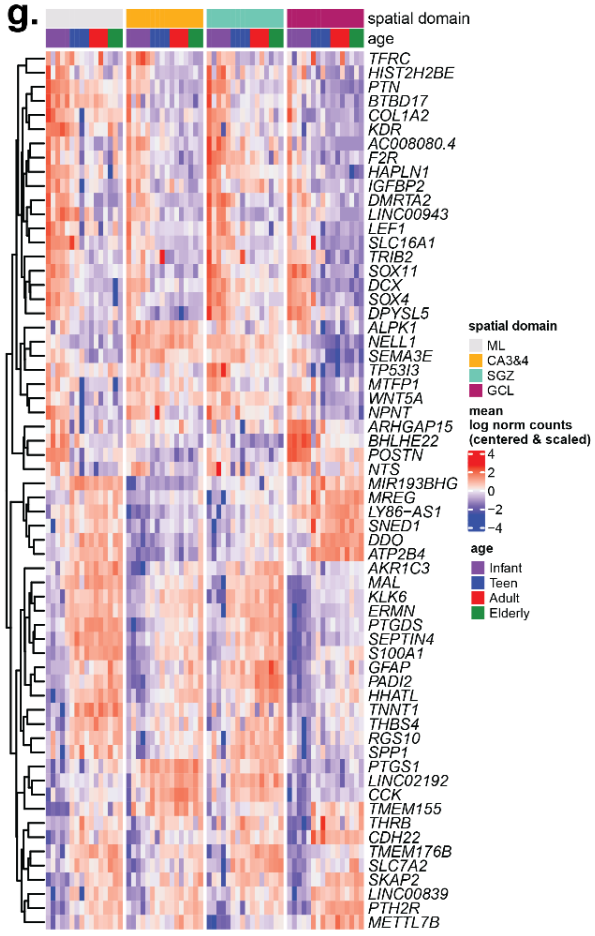

Figure 3. Differential gene expression of infant versus non-infant in sub-domains of the DG. (**a-d**) Volcano plots of infant versus non-infant for individual spatial domains: ML (**a**), GCL (**b**), SGZ (**c**) and CA3&4 (**d**). The *x*-axis is the $\log_2$ fold change in expression and the *y*-axis is the negative $\log_{10}$ adjusted *p*-values. (**e**) Representative smFISH images of coronal sections for the infant GCL (top row) and adult GCL (bottom row) for the following genes: *PROX1* (green), *SLC17A7* (magenta), *GAD1* (yellow), and *LAMP5* (white). Scale bar is 100 µm. (**f**) Stacked barplot of the number of differentially expressed genes (DEGs) for each spatial domain of the dentate gyrus (DG), stacked by age group. X-axis on log scale. (**g**) Heatmap of the mean $\log_2$ normalized counts (centered and scaled) for top 10 enriched and depleted genes with ≥1.5 logFC or ≤-1.5 logFC from each spatial domain. Pseudo-bulked data limited to the spatial domains of the DG. Hierarchical clustering was performed across rows. Columns are organized by spatial domains corresponding to DG regions.

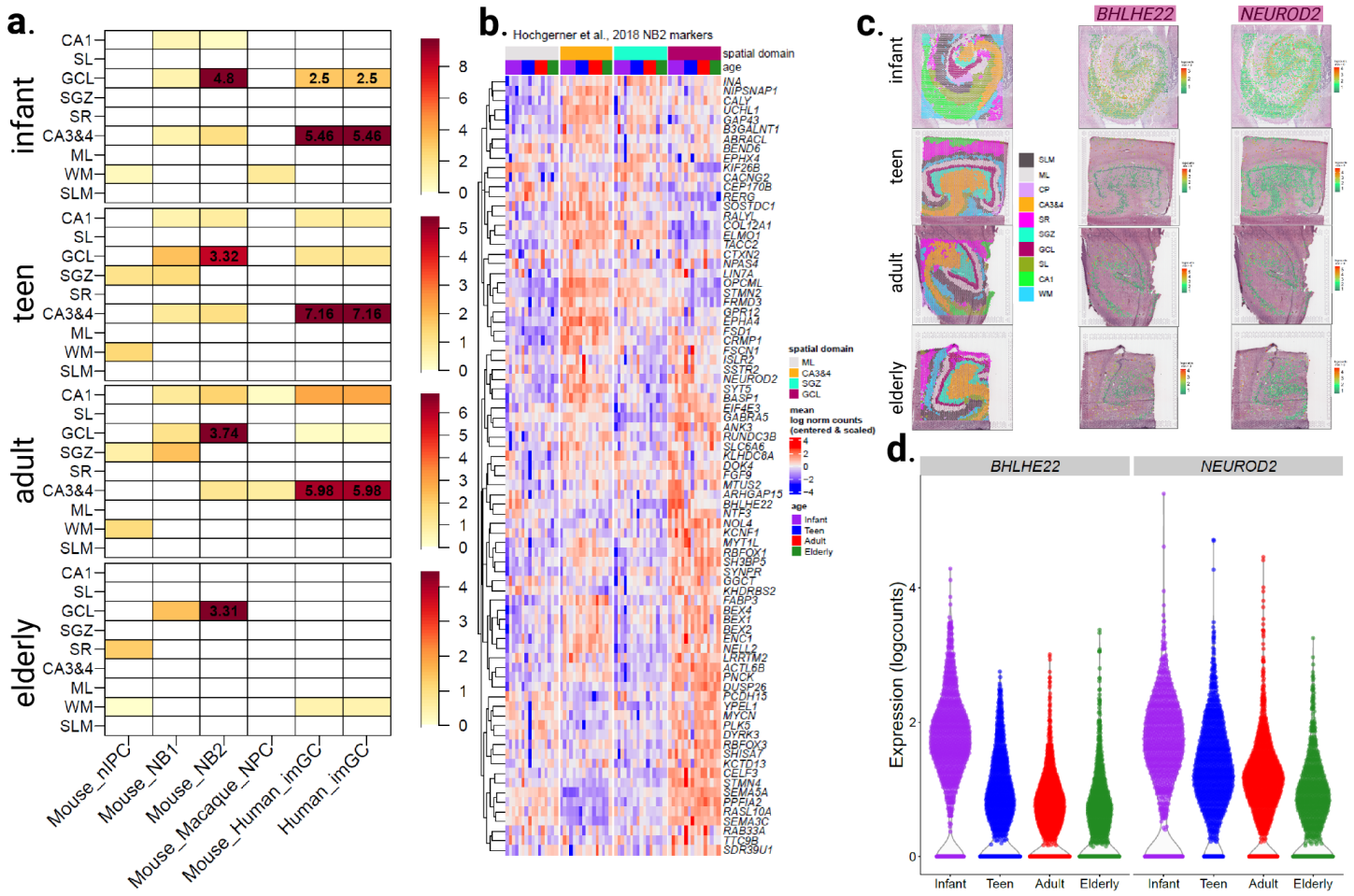

Figure 4. Late stage mouse neuroblast gene signature is enriched in the GCL across the lifespan. (**a**) Enrichment analyses using Fisher's exact tests for predefined gene sets for neural precursor cells (nIPC and NPC), neuroblasts (NB1 and NB2), and immature granular cells (imGC). Nomenclature was adopted from each publication [18,19,67]. Color indicates negative $\log_{10}$ *p*-values while numbers within each significant heatmap cell indicates the odds ratios for the enrichment. (**b**) Heatmap of the mean $\log_2$ normalized counts (centered and scaled) for the NB2 gene set [18] on pseudo-bulked data limited to the spatial domains of the DG. Hierarchical clustering was performed across rows. Columns are organized by spatial domains corresponding to DG regions. (**c**) Data visualization of the Visium spots of mean $\log_2$ normalized counts four representative samples from each age group (rows from top to bottom: infant (Br8533), teen (Br1412), adult (Br3942), elderly (Br6023)) for spatial domain (1st column), *BHLHE22* (2nd column), and *NEUROD2* (3rd column). Spots in the1st column are colored by spatial domain, while in 2nd and 3rd columns, spots are colored by logcounts of the respective gene. (**d**) Violin plots of *BHLHE22* and *NEUROD2* for GCL Visium spots. *X*-axis are age groups and *y*-axis are logcounts.

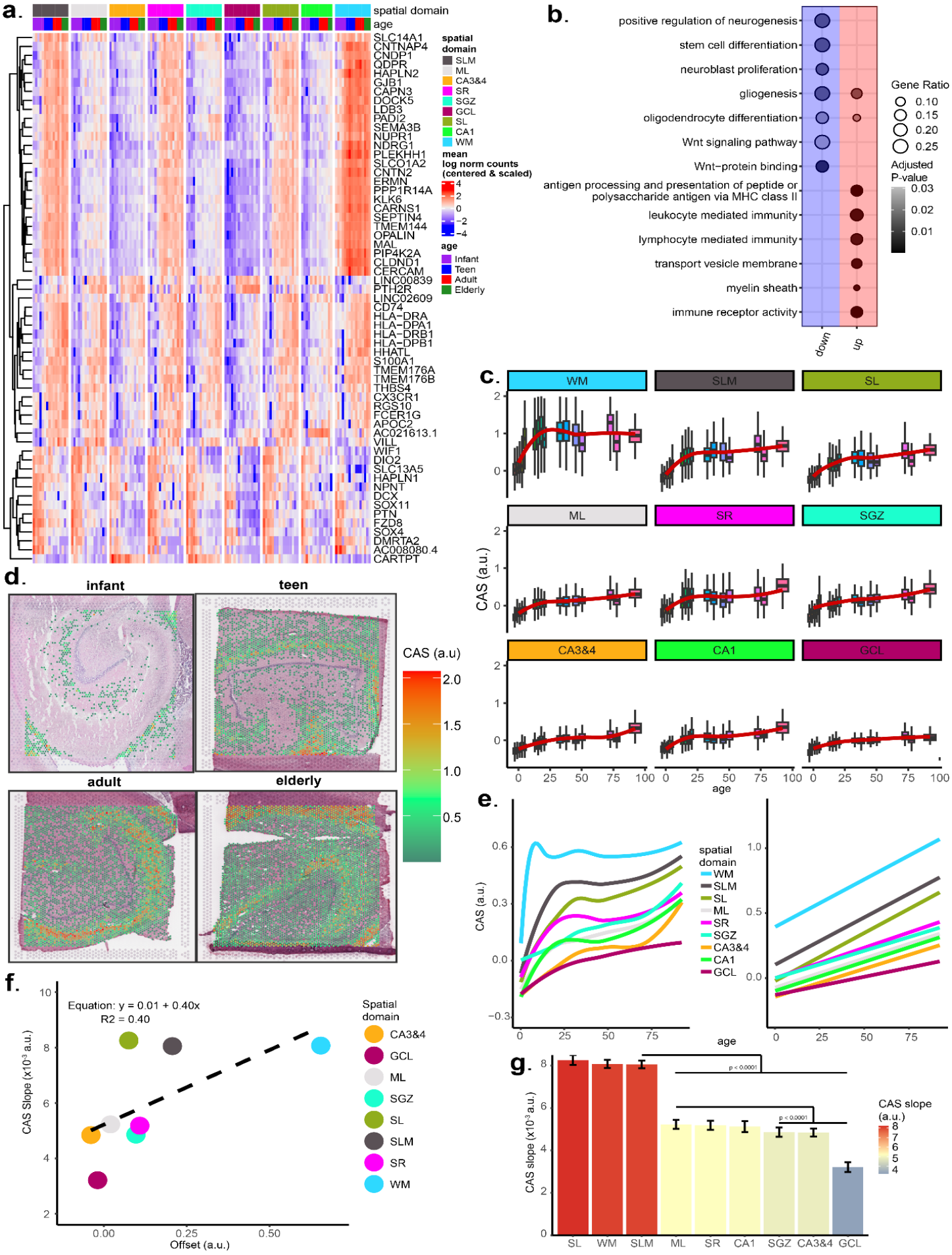

Figure 5. Wide-spread HPC aging signature identifies regions of local tissue that change more with age. (**a**) Heatmap of the mean $\log_2$ normalized counts (centered and scaled) for the wide-spread aging signature gene set. Hierarchical clustering was performed across rows. Columns are organized by spatial domains corresponding to HPC spatial domains. Labeled genes are those that show strong increasing age gradients across many spatial domains. (**b**) Dot plot for major gene ontology terms from aging signature gene set. Dot plots are faceted by their down- and up-regulation columns colored by blue and red, respectively; dot size represents the fraction of gene set that was differentially expressed (Gene ratio), while black gradient represents adjusted p-value. (**c**) Boxplots of CAS (in arbitrary units) of individual Visium spots versus age, faceted by HPC spatial domain and fitted with LOESS line. (**d**) Data visualization of the Visium spots for four representative samples from each age group (infant (Br8533), teen (Br1412), adult (Br3942), elderly (Br5242)). Color of spots are for CAS in arbitrary units. (**e**) CAS trajectories of all HPC spatial domains vs. age approximated via LOESS and linear regression. (**f**) Offset of linear fit and slope comparison from linear modeling of CAS across all Visium spots. (**g**) CAS slope of linear approximations in **e**, colored by slope, for each spatial domain. Mean ± 95% confidence intervals. Adjusted *p*-values derived from two-sided Tukey's HSD test.

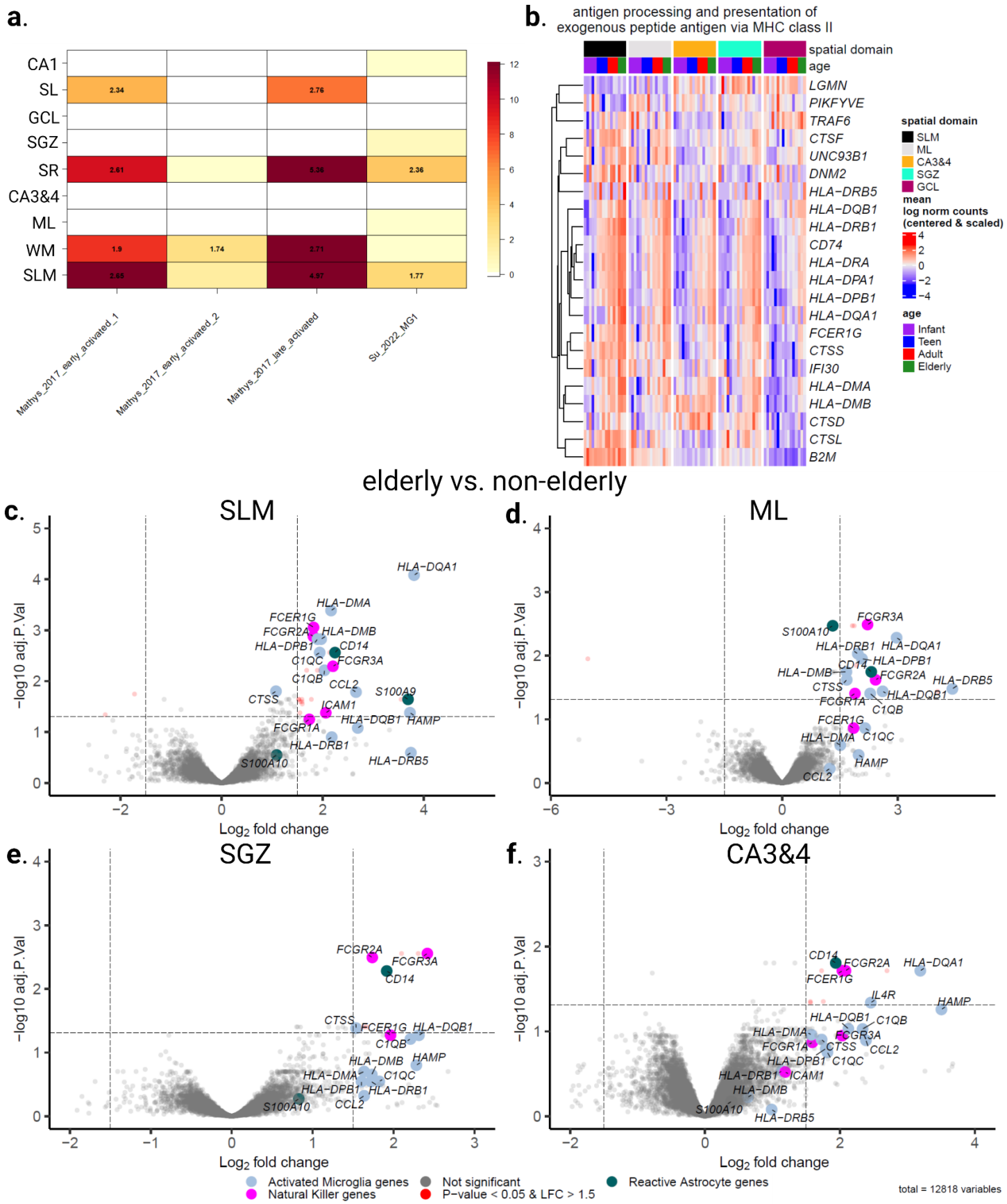

Figure 6. Expression of inflammatory markers enriched in SLM, ML, SGZ, and CA3&4 domains in elderly age group. (**a**) Enrichment analyses using Fisher's exact tests for predefined gene sets for activated microglial markers. Nomenclature adopted from each publication: microglial clusters for early_activated_1, early_activated_2, late_activated [49], and human microglial cluster 1 (MG1) [73]. Color indicates negative $\log_{10}$ *p*-values while numbers within significant heatmap cells indicate odds ratios for the enrichments. (**b**) Heatmap of the mean $\log_2$ normalized counts (centered and scaled) of pseudo-bulked data limited to the SLM and spatial domains of

the DG with genes, which satisfy gene ontology accession GO:0002504. Hierarchical clustering was performed across all rows. Columns are organized by spatial domains corresponding to DG regions and the SLM, and by age-group. (**c-f**) Volcano plots of elderly vs. non-elderly for individual spatial domains: SLM (**c**), ML (**d**), SGZ (**e**) and CA3&4 (**f**). The *x*-axis is the $\log_2$ fold change in expression and the *y*-axis is the negative $\log_{10}$ adjusted *p*-values.

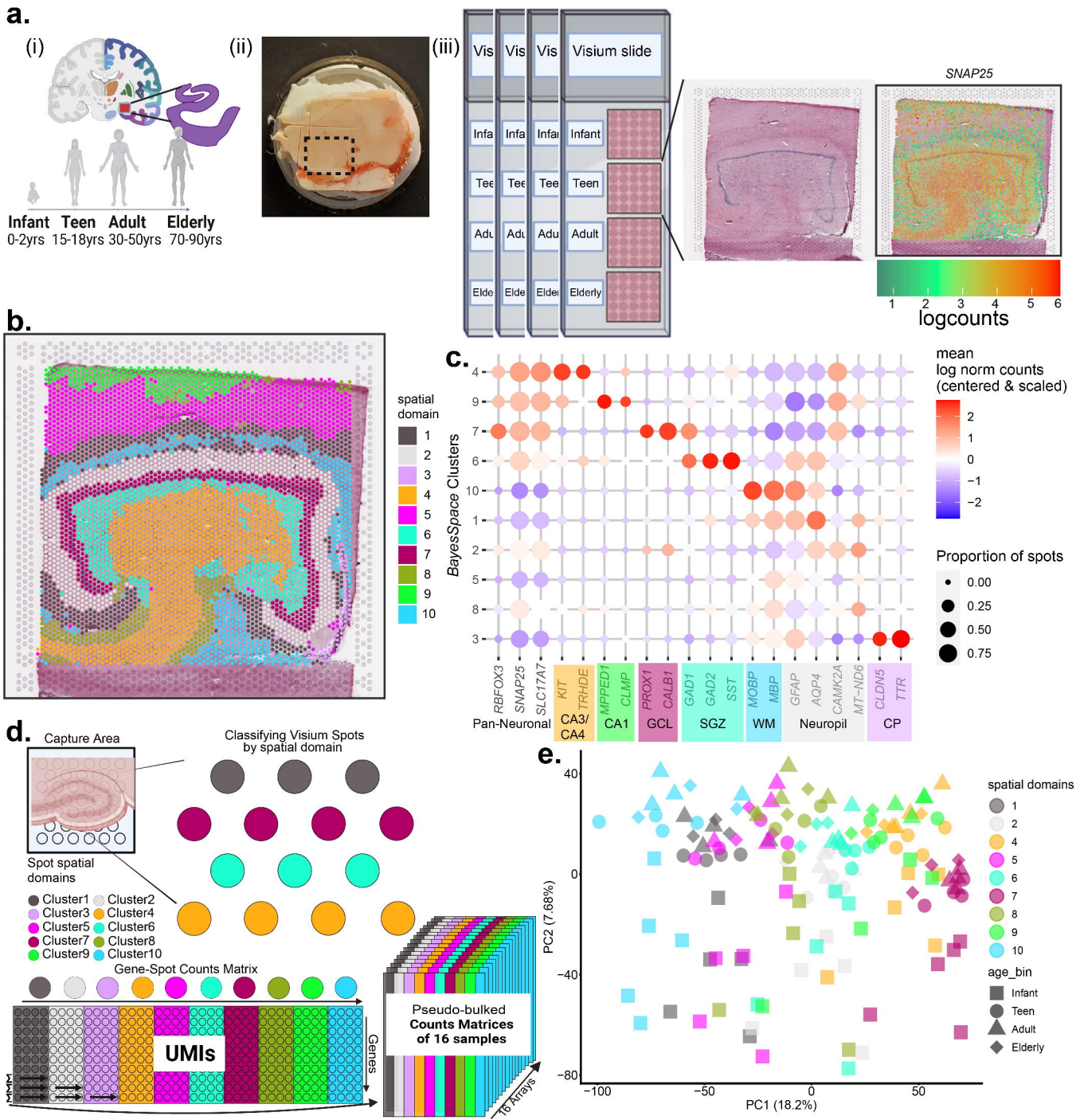
a.
(i)
(ii)
(iii)
Infant Teen Adult Elderly
0-2yrs 15-18yrs 30-50yrs 70-90yrs
Visium slide
Infant
Teen
Adult
Elderly
SNAP25
logcounts
b.
spatial domain
c.
BayesSpace Clusters
mean log norm counts (centered & scaled)
Proportion of spots
RBFOX3
SNAP25
SLC17A7
KIT
TRHDE
MPPED1
CLMP
PROX1
CALB1
GAD1
GAD2
SST
MOBP
MBP
GFAP
AQP4
CAMK2A
MT-ND6
CLDN5
TTR
Pan-Neuronal
CA3/ CA4
CA1
GCL
SGZ
WM
Neuropil
CP
d.
Capture Area
Classifying Visium Spots by spatial domain
Spot spatial domains
Cluster1
Cluster2
Cluster3
Cluster4
Cluster5
Cluster6
Cluster7
Cluster8
Cluster9
Cluster10
Gene-Spot Counts Matrix
UMIs
Genes
Pseudo-bulked Counts Matrices of 16 samples
16 Arrays
e.
PC1 (18.2%)
PC2 (7.68%)
spatial domains
age_bin
Infant
Teen
Adult
Elderly

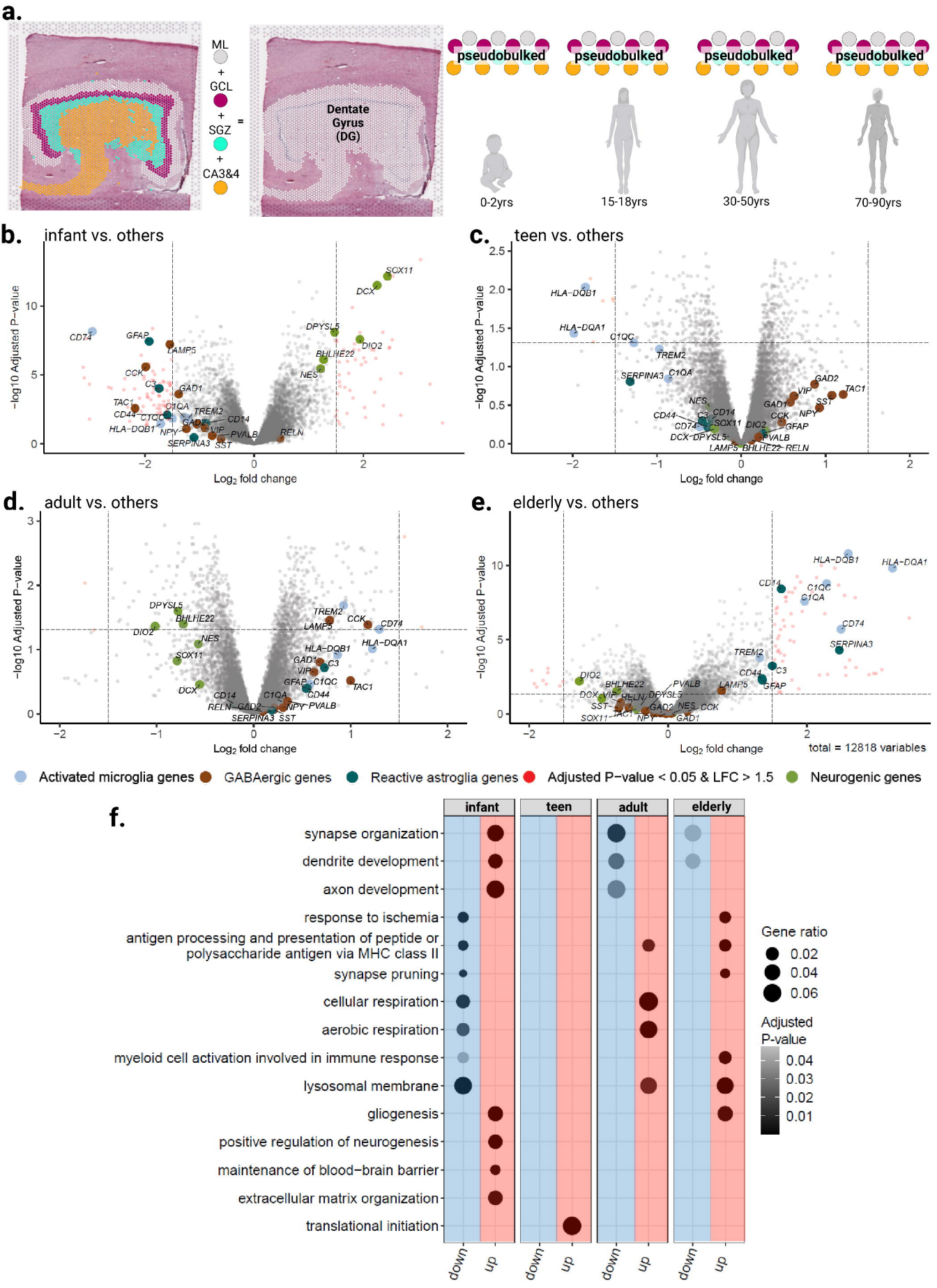
a.
ML
+
GCL
+
SGZ
+
CA3&4
=
Dentate Gyrus (DG)
pseudobulked
pseudobulked
pseudobulked
pseudobulked
0-2yrs
15-18yrs
30-50yrs
70-90yrs
b.
infant vs. others
c.
teen vs. others
d.
adult vs. others
e.
elderly vs. others
−log10 Adjusted P−value
Log2 fold change
total = 12818 variables
Activated microglia genes
GABAergic genes
Reactive astroglia genes
Adjusted P−value < 0.05 & LFC > 1.5
Neurogenic genes
f.
infant
teen
adult
elderly
synapse organization
dendrite development
axon development
response to ischemia
antigen processing and presentation of peptide or polysaccharide antigen via MHC class II
synapse pruning
cellular respiration
aerobic respiration
myeloid cell activation involved in immune response
lysosomal membrane
gliogenesis
positive regulation of neurogenesis
maintenance of blood−brain barrier
extracellular matrix organization
translational initiation
down
up
Gene ratio
0.02
0.04
0.06
Adjusted P-value
0.04
0.03
0.02
0.01

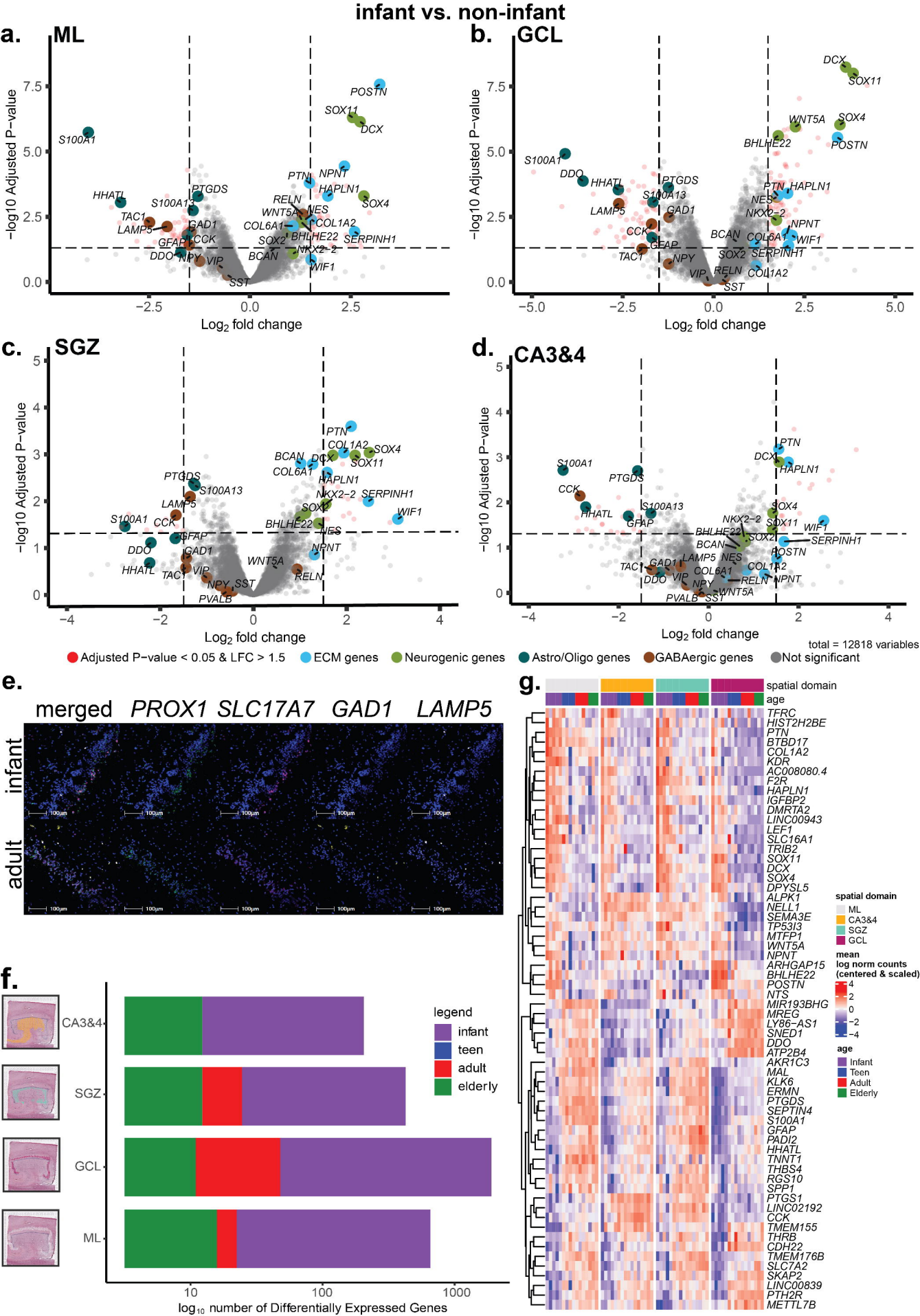
infant vs. non-infant
a.
ML
b.
GCL
c.
SGZ
d.
CA3&4
−log10 Adjusted P−value
Log2 fold change
Adjusted P−value < 0.05 & LFC > 1.5
ECM genes
Neurogenic genes
Astro/Oligo genes
GABAergic genes
Not significant
total = 12818 variables
e.
merged
PROX1
SLC17A7
GAD1
LAMP5
infant
adult
f.
CA3&4
SGZ
GCL
ML
legend
infant
teen
adult
elderly
log10 number of Differentially Expressed Genes
g.
spatial domain
age
mean
log norm counts
(centered & scaled)
Infant
Teen
Adult
Elderly

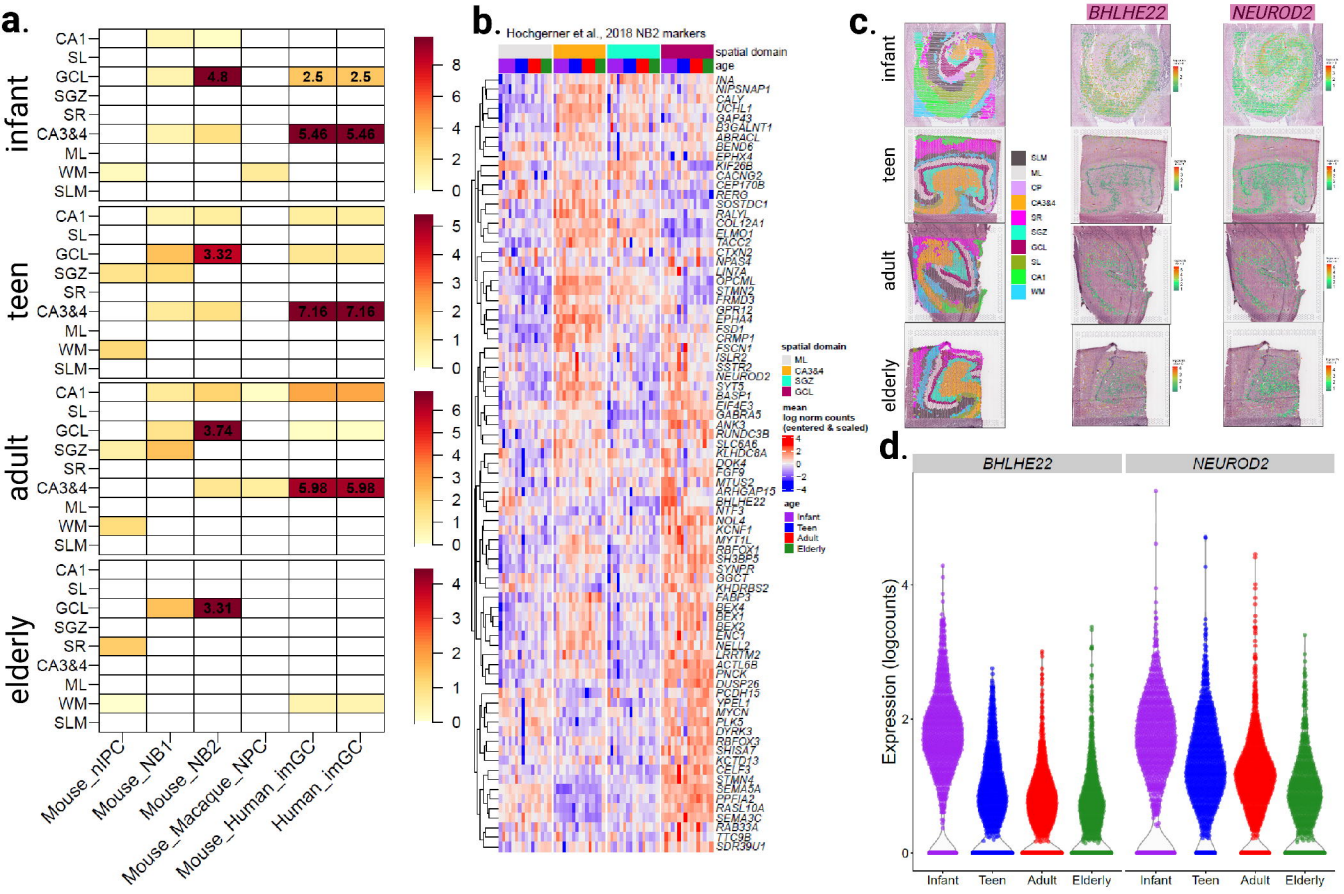
a.
infant
teen
adult
elderly
CA1
SL
GCL
SGZ
SR
CA3&4
ML
WM
SLM
4.8
2.5
2.5
3.32
7.16
7.16
3.74
5.98
5.98
3.31
Mouse_nIPC
Mouse_NB1
Mouse_NB2
Mouse_Macaque_NPC
Mouse_Human_imGC
Human_imGC
b.
Hochgerner et al., 2018 NB2 markers
spatial domain
age
INA
NIPSNAP1
CALY
DCTL1
GAP43
B3GALNT1
ABRACL
BEND6
EPHX4
KIF26B
CACNG2
CEP170B
RERG
SOSTDC1
RALYL
COL12A1
ELMO1
TACC2
CTXND
NPAS4
LINTA
OPCML
TMMX2
FRMD3
GPR12
EPHA4
FSD1
CRMP1
FSCN1
ISLR2
SSTR2
NEUROD2
SYT3
BASP1
EIF4E2
GABRA5
ANK3
RUNDC3B
SLC6A6
KLHDC8A
DOK4
FTR9
MTUS2
ARHGAP15
BHLHE22
NTN3
NOL4
KCNF1
MYT1L
RBFOX1
SH3BP5
SYNDR
GGCT
KHDRBS2
FABP3
BEX4
BEX1
BEX2
ENC1
NELL2
LRRTM2
ACTL6B
PNCK
DUSP26
PCDH15
YPEL1
MYCN
PLK5
DYRK3
FBXO33
SHISA7
KCTD13
CELF4
STMN4
SEMA5A
DPF1A2
RASL10A
SEMA3C
RAB33A
TTC9B
SDR39U1
spatial domain
ML
CA3&4
SGZ
GCL
mean
log norm counts
(centered & scaled)
age
Infant
Teen
Adult
Elderly
c.
BHLHE22
NEUROD2
infant
teen
adult
elderly
SLM
ML
CP
CA3&4
SR
SGZ
GCL
SL
CA1
WM
d.
BHLHE22
NEUROD2
Expression (logcounts)
Infant
Teen
Adult
Elderly

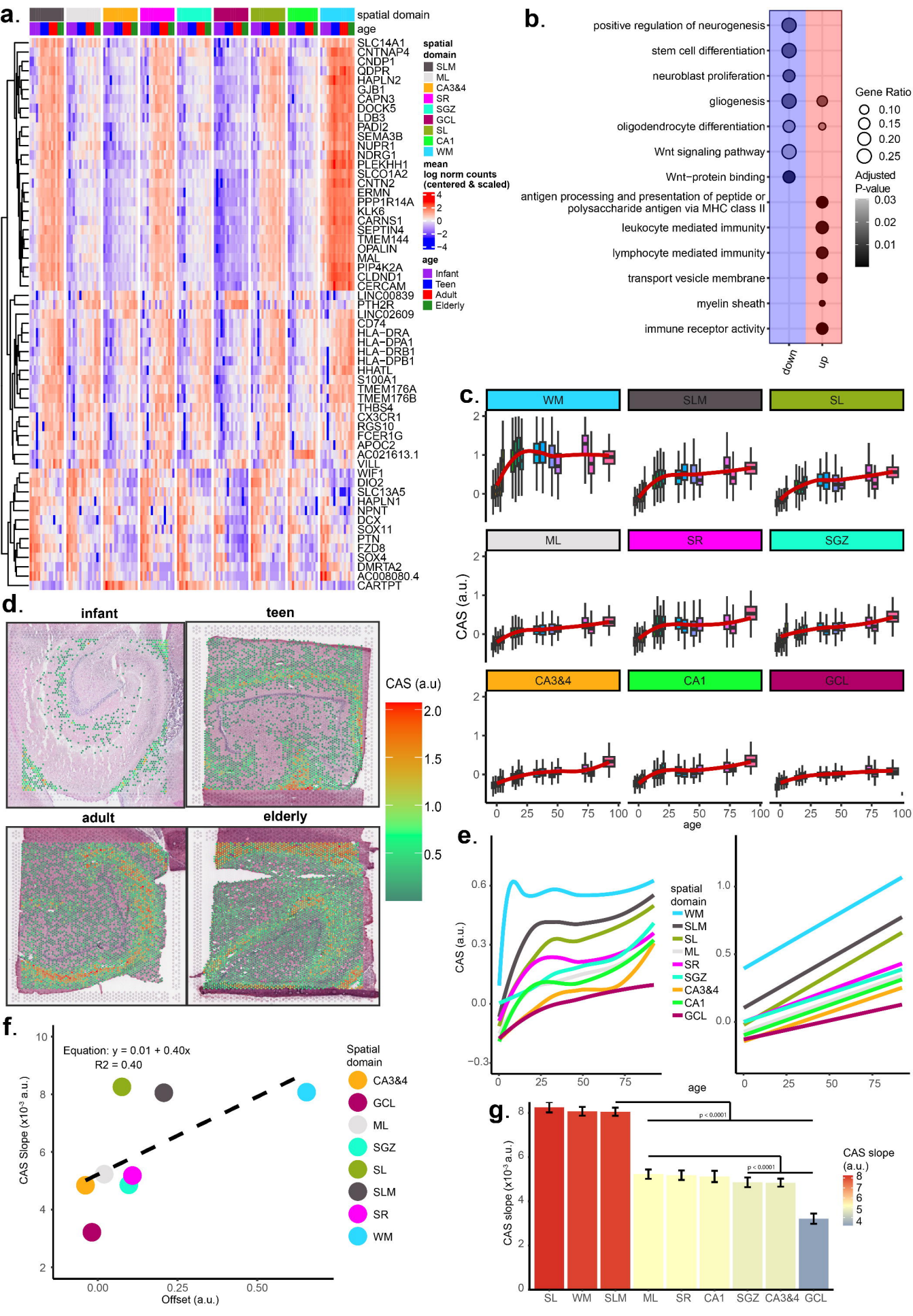
a.
spatial domain
age
SLC14A1
CNTNAP4
CNDP1
QDPR
HAPLN2
GJB1
CAPN3
DOCK5
LDB3
PADI2
SEMA3B
NUPR1
NDRG1
PLEKHH1
SLCO1A2
CNTN2
ERMN
PPP1R14A
KLK6
CARNS1
SEPTIN4
TMEM144
OPALIN
MAL
PIP4K2A
CLDND1
CERCAM
LINC00839
PTH2R
LINC02609
CD74
HLA-DRA
HLA-DPA1
HLA-DRB1
HLA-DPB1
HHATL
S100A1
TMEM176A
TMEM176B
THBS4
CX3CR1
RGS10
FCER1G
APOC2
AC021613.1
VILL
WIF1
DIO2
SLC13A5
HAPLN1
NPNT
DCX
SOX11
PTN
FZD8
SOX4
DMRTA2
AC008080.4
CARTPT
spatial domain
SLM
ML
CA3&4
SR
SGZ
GCL
SL
CA1
WM
mean log norm counts (centered & scaled)
4
2
0
−2
−4
age
Infant
Teen
Adult
Elderly
b.
positive regulation of neurogenesis
stem cell differentiation
neuroblast proliferation
gliogenesis
oligodendrocyte differentiation
Wnt signaling pathway
Wnt−protein binding
antigen processing and presentation of peptide or polysaccharide antigen via MHC class II
leukocyte mediated immunity
lymphocyte mediated immunity
transport vesicle membrane
myelin sheath
immune receptor activity
down
up
Gene Ratio
0.10
0.15
0.20
0.25
Adjusted P-value
0.03
0.02
0.01
c.
WM
SLM
SL
ML
SR
SGZ
CA3&4
CA1
GCL
CAS (a.u.)
age
d.
infant
teen
adult
elderly
CAS (a.u)
2.0
1.5
1.0
0.5
e.
CAS (a.u.)
spatial domain
WM
SLM
SL
ML
SR
SGZ
CA3&4
CA1
GCL
age
f.
Equation: y = 0.01 + 0.40x
R2 = 0.40
CAS Slope (x10⁻³ a.u.)
Offset (a.u.)
Spatial domain
CA3&4
GCL
ML
SGZ
SL
SLM
SR
WM
g.
CAS slope (x10⁻³ a.u.)
p < 0.0001
p < 0.0001
CAS slope (a.u.)
SL
WM
SLM
ML
SR
CA1
SGZ
CA3&4
GCL

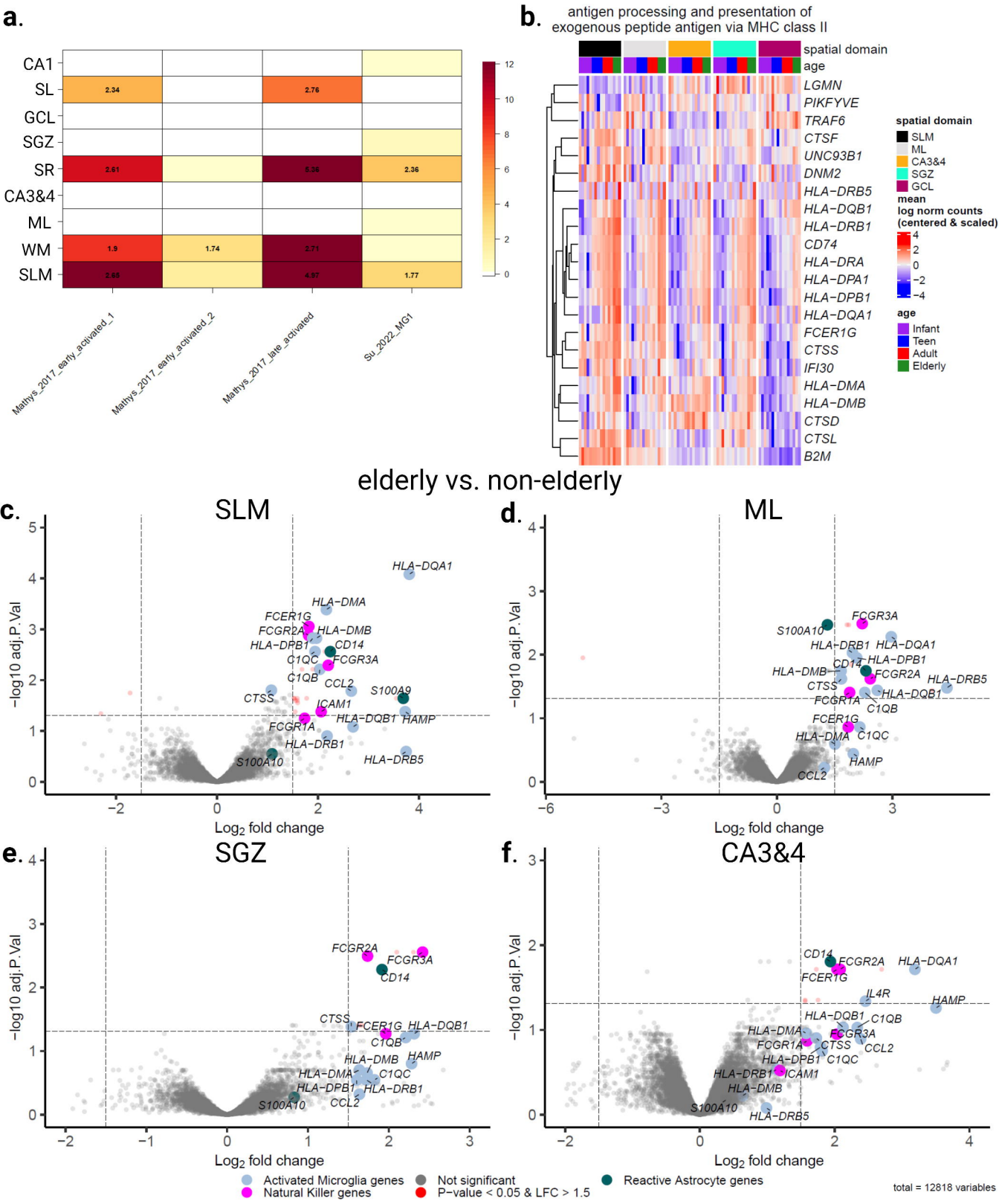
a.
CA1
SL
GCL
SGZ
SR
CA3&4
ML
WM
SLM
2.34
2.76
2.61
5.36
2.36
1.9
1.74
2.71
2.65
4.97
1.77
12
10
8
6
4
2
0
Mathys_2017_early_activated_1
Mathys_2017_early_activated_2
Mathys_2017_late_activated
Su_2022_MG1
b.
antigen processing and presentation of exogenous peptide antigen via MHC class II
spatial domain
age
LGMN
PIKFYVE
TRAF6
CTSF
UNC93B1
DNM2
HLA-DRB5
HLA-DQB1
HLA-DRB1
CD74
HLA-DRA
HLA-DPA1
HLA-DPB1
HLA-DQA1
FCER1G
CTSS
IFI30
HLA-DMA
HLA-DMB
CTSD
CTSL
B2M
spatial domain
SLM
ML
CA3&4
SGZ
GCL
mean log norm counts (centered & scaled)
4
2
0
−2
−4
age
Infant
Teen
Adult
Elderly
elderly vs. non-elderly
c.
SLM
−log10 adj.P.Val
Log2 fold change
HLA-DQA1
HLA-DMA
FCER1G
FCGR2A
HLA-DMB
HLA-DPB1
CD14
C1QC
FCGR3A
C1QB
CCL2
S100A9
CTSS
ICAM1
HLA-DQB1
HAMP
FCGR1A
HLA-DRB1
S100A10
HLA-DRB5
d.
ML
−log10 adj.P.Val
Log2 fold change
FCGR3A
S100A10
HLA-DRB1
HLA-DQA1
CD14
HLA-DPB1
HLA-DMB
FCGR2A
HLA-DRB5
CTSS
HLA-DQB1
FCGR1A
C1QB
FCER1G
HLA-DMA
C1QC
HAMP
CCL2
e.
SGZ
−log10 adj.P.Val
Log2 fold change
FCGR2A
FCGR3A
CD14
CTSS
FCER1G
HLA-DQB1
C1QB
HLA-DMB
HAMP
HLA-DMA
C1QC
HLA-DPB1
HLA-DRB1
CCL2
S100A10
f.
CA3&4
−log10 adj.P.Val
Log2 fold change
CD14
FCGR2A
HLA-DQA1
FCER1G
IL4R
HAMP
HLA-DQB1
C1QB
HLA-DMA
FCGR3A
FCGR1A
CTSS
CCL2
HLA-DPB1
C1QC
HLA-DRB1
ICAM1
HLA-DMB
S100A10
HLA-DRB5
Activated Microglia genes
Natural Killer genes
Not significant
P-value < 0.05 & LFC > 1.5
Reactive Astrocyte genes
total = 12818 variables